TURBULENT FLOW AND ACOUSTIC PREDICTIONS OVER OPEN CAVITY CONFIGURATIONS AT TRANSONIC SPEEDS

A THESIS SUBMITTED TO
THE GRADUATE SCHOOL OF NATURAL AND APPLIED SCIENCES
OF
MIDDLE EAST TECHNICAL UNIVERSITY

BY

SEYFETTIN ÇOŞKUN

IN PARTIAL FULFILLMENT OF THE REQUIREMENTS
FOR
THE DEGREE OF MASTER OF SCIENCE
IN
AEROSPACE ENGINEERING

JUNE 2019

Approval of the thesis:

TURBULENT FLOW AND ACOUSTIC PREDICTIONS OVER OPEN CAVITY CONFIGURATIONS AT TRANSONIC SPEEDS

submitted by **SEYFETTIN ÇOŞKUN** in partial fulfillment of the requirements for the degree of **Master of Science in Aerospace Engineering Department, Middle East Technical University** by,

Prof. Dr. Halil Kalıpçılar
Dean, Graduate School of **Natural and Applied Sciences**

Prof. Dr. İsmail Hakkı Tuncer
Head of Department, **Aerospace Engineering**

Prof. Dr. Yusuf Özyörük
Supervisor, **Aerospace Engineering, METU**

Examining Committee Members:

Prof. Dr. İsmail Hakkı Tuncer
Aerospace Engineering, METU

Prof. Dr. Yusuf Özyörük
Aerospace Engineering, METU

Prof. Dr. Serkan Özgen
Aerospace Engineering, METU

Prof. Dr. Nafiz Alemdaroğlu
School of Civil Aviation, Atılım University

Dr. Munir Elfarra
Aerospace Engineering, Ankara Yıldırım Beyazıt University

Date:

I hereby declare that all information in this document has been obtained and presented in accordance with academic rules and ethical conduct. I also declare that, as required by these rules and conduct, I have fully cited and referenced all material and results that are not original to this work.

Name, Surname: Seyfettin Çoşkun

Signature :

ABSTRACT

TURBULENT FLOW AND ACOUSTIC PREDICTIONS OVER OPEN CAVITY CONFIGURATIONS AT TRANSONIC SPEEDS

Çoşkun, Seyfettin
M.S., Department of Aerospace Engineering
Supervisor: Prof. Dr. Yusuf Özyörük

June 2019, 79 pages

In modern military fighters, internal carriage of weapons is vital in terms of high survivability, low observability and aerodynamic performance of the fighter. During store release phases of operation, the aircraft will have to fly with the cavity exposed to free stream conditions. When an aircraft internal weapons bay is exposed to free stream of air, a highly unsteady and complex flow field develops within the cavity. This triggers intense aero-acoustic environment in and around the cavity. Highly complex, unsteady and nonlinear flow environment of a cavity may cause possible structural, acoustic and aerodynamic problems such as fatigue in structures, nose-up pitching moment on stores, resonance in cavity walls and etc. Therefore, it is desired to assure that internal stores, aircraft structures and internal weapon bay (IWB) structure and equipment inside the IWB can withstand this harsh environment to successfully complete the mission under required conditions.

In this respect, various cavity configurations such as clean cavity (i.e. no stores, no doors etc.), cavity with a generic store, cavity with doors and doors at different orientations are analyzed for the effects of each configuration on cavity acoustic characteristics. Unsteady Reynolds-Averaged (URANS) and Detached Eddy Simulation (DES) turbulence model variants available in ANSYS/Fluent solver are utilized. It has been found out that although URANS models can predict the OASPL trends within the cavity with a level of accuracy, they are lack of accuracy in capturing the frequency spectra due to averaging nature of URANS models. On the other hand, IDDES model is quite successful in predicting both the noise intensity and the frequency spectra of various cavity configurations at transonic speeds.

Keywords: internal weapons bays, aeroacoustics, computational fluid dynamics, cavity flow

ÖZ

TRANSONİK HIZLARDAKİ AÇIK KAVİTE KONFİGÜRASYONLARININTÜRBÜLANSLI AKIŞ VE AKUSTİK TAHMİNİ

Çoşkun, Seyfettin
Yüksek Lisans, Havacılık ve Uzay Mühendisliği Bölümü
Tez Yöneticisi: Prof. Dr. Yusuf Özyörük

Haziran 2019 , 79 sayfa

Modern savaş uçaklarında mühimmatların gövde içinde taşınması, uçağın düşük görünürlüğü, bekası ve aerodinamik performansı için yüksek öneme sahiptir. Operasyonda mühimmat ayrılması sırasında, uçak dahili silah yuvası serbest akışa maruz kalır. Dahili silah yuvasının serbest akışa maruz kalmasıyla silah yuvasında ve çevresinde yüksek derecede kararsız ve karmaşık bir akış meydana gelir ve oluşan girdapsal yapılar silah yuvası duvarları ve kayma tabakası ile etkileşime girer. Bu etkileşim silah yuvasında ve çevresinde yoğun aeroakustik bir ortama sebep olur. Fazlaca karmaşık, kararsız ve doğrusal olmayan akış ortamı yapısal yorulma, mühimmatlarda burun yukarı moment oluşumu, kavite duvarlarında rezonans vb. muhtemel yapısal, aeroakustik ve aerodinamik problemlere sebep olabilir. Bunlara ek olarak kavite içindeki akustik basınç alanı yüksek yoğunluklu akustik tonlar oluşmasına da sebep olabilir ki bu durum yapısal ve kavite etrafındaki sistemler için zarar verici olabilir. Bu sebeple, harekat sırasında dahili mühimmatların, uçak yapılarının, dahili silah yuvası ve teçhizatlarının kavite çevresinde gelişen zorlu ortama dayanabilmesi gerekir. Bütün sistemler ve yapılar gerçek harekat koşullarını yansıtan akustik ortama dayanıklılık için vasıflandırılmalıdır.

Bu bakımdan, boş kavite, mühimmat içeren kavite, kapakların bulunduğu kavite gibi farklı kavite konfigürasyonları analiz edilerek incelenen konfigürasyonların kavite akustik karakteristiği üzerindeki etkileri incelenmiştir. ANSYS/Fluent ticari hesaplamalı akışkanlar dinamiği (HAD) çözücüsünde bulunan URANS ve DES modelleriye çözümler yapılmıştır. URANS modelleri ortalama alma doğaları gereği kavite akustiğinin tahmin edilmesinde yeterli doğruluk sağlayamamıştır. IDDES modeli ise farklı kavite konfigürasyonlarının frekans spektrumu ve gürültü yoğunluğu tahmininde beklenen doğrulukta sonuçlar sağlamıştır.

Anahtar Kelimeler: dahili silah yuvası, aeroakustik, hesaplamalı akışkanlar dinamiği, kavite akışı

To my family ...

ACKNOWLEDGMENTS

Öncelikle bu çalışma sürecinde ufkumu açan, yol gösteren ve yardımlarını hiçbir zaman esirgemeyen değerli hocam, tez danışmanım Prof. Dr. Yusuf Özyörük'e sonsuz teşekkürlerimi sunarım.

Eğitim hayatım boyunca yanımda olan, desteklerini asla esirgemeyen ve bana her zaman inanan aileme çok teşekkür ederim.

Ayrıca sağladığı hesaplama platformu desteği için Türk Havacılık Uzay Sanayii'ne teşekkür ederim.

TABLE OF CONTENTS

ABSTRACT v

ÖZ vii

ACKNOWLEDGMENTS x

TABLE OF CONTENTS xi

LIST OF TABLES xv

LIST OF FIGURES xvi

LIST OF ABBREVIATIONS xx

CHAPTERS

1 INTRODUCTION 1

1.1 Description of the Problem 1

1.1.1 Cavity Flow Types 2

1.1.1.1 Closed Cavity Flows 4

1.1.1.2 Open Cavity Flows 5

1.1.1.3 Transitional Cavity Flows 6

1.2 Literature Search 6

1.3 The Objectives of The Thesis 7

1.4 The Scope of The Thesis 8

2 GOVERNING EQUATIONS OF FLUID DYNAMICS AND NUMERICAL METHODS 9
2.1 Navier-Stokes Equations 9
2.2 Turbulence Modelling 10
2.2.1 Resolution Requirements 12
2.2.2 Large Eddy Simulation (LES) 13
2.2.3 Unsteady Reynolds-Averaged Navier-Stokes (URANS) Modelling 13
2.2.3.1 Reynolds Decomposition 13
2.2.3.2 URANS Equations 14
2.2.3.2.1 k-ω Shear Stress Transport (SST) Two-Equation Model 15
2.2.3.2.2 RNG k-ϵ Two-Equation Model 15
2.2.4 Detached Eddy Simulation (DES) 16
2.2.4.1 Classical Detached Eddy Simulation (DES) 16
2.2.4.2 Issues in DES 17
2.2.4.3 Delayed Detached Eddy Simulation (DDES) 18
2.2.4.4 Improved-Delayed Detached Eddy Simulation (IDDES) 18
2.3 Acoustics 20
2.3.1 Ffowcs Williams – Hawkings (FWH) Acoustic Analogy 20
2.3.2 Acoustic Data Processing 23
2.3.2.1 Overall Sound Pressure Level (OASPL) 24
2.3.2.2 Spectral Analyses and Fast Fourier Transform (FFT) . . 24
2.3.2.3 Rossiter Modes 25

3 ASSESSMENT OF TURBULENT FLOW MODELS FOR CAVITY FLOWS 27

3.1 CFD Validation Test Case: M219 Cavity 27

3.2 URANS Models in Cavity Flow Solutions 29

3.2.1 Computational Domain 29

3.2.2 Grid Independency 30

3.2.3 Effects of Order of Spatial Discretization Scheme 32

3.3 Detached Eddy Simulations in Cavity Flow Solutions 34

3.3.1 Effects of Detached Eddy Simulation Variants 34

3.3.2 Grid Independency 35

3.3.3 Effects of Time-step 36

3.3.4 Turbulence Models Comparison for Cavity Flow Solutions . . 39

4 RESULTS AND DISCUSSION 41

4.1 Cavity Configurations 41

4.1.1 Clean Cavity Flow 41

4.1.2 Cavity With A Generic Store 46

4.1.3 Door Effects On Cavity Flow 49

4.1.3.1 Doors at 90° Orientation 49

4.1.3.2 Doors Orientation Effects 52

4.1.4 Reynolds Number Dependency of Cavity Flows 58

4.2 Farfield Noise Prediction By Ffowcs Williams - Hawkings Acoustic Analogy 59

5 CONCLUSIONS 61

Appendix A GRID SIZE AND COMPUTATIONAL COST APPROXIMATIONS FOR DNS AND LES 65

A.1 DNS Resolution 65

A.2 LES Resolution for Wall Bounded Flows 65

A.2.1 Outer Layer 66

A.2.2 Inner Layer 66

Appendix B TURBULENCE MODELS DETAILS 67

B.1 URANS Additional Equations 67

B.2 k-ω SST Turbulence Model Additional Equations and Model Constants 68

B.3 RNG k-ϵ Turbulence Model Additional Equations and Model Constants 68

B.4 Sutherland's Law of Dynamic Viscosity 69

B.5 Spalart-Almaras (S-A) One-Equation Turbulence Model 70

Appendix C DATA PROCESSING DETAILS 73

C.1 Fast Fourier transform (FFT) 73

C.2 Windowing 73

REFERENCES 77

LIST OF TABLES

TABLES

Table 3.1 Parameters for URANS Grid Convergence Study 30

Table 3.2 Parameters for IDDES Grid Convergence Study 36

LIST OF FIGURES

FIGURES

Figure 1.1 Acoustic feedback loop within the cavity 2

Figure 1.2 Cavity flow type characterization based on cavity baseline pressure distributions [1] 3

Figure 1.3 Typical acoustic spectrum in closed cavity flows. 4

Figure 1.4 Nose-up pitching moment induced closed cavity flow on a store in the cavity. 4

Figure 1.5 Typical modal spectrum of open cavity flows. 5

Figure 2.1 Turbulence models classification [2] 11

Figure 2.2 Resolution requirements of DNS, LES, and RANS (modified from Piomelli [3]) 12

Figure 2.3 Reynolds decomposition of turbulent quantities 14

Figure 2.4 FW-H control surface definition 22

Figure 2.5 FW-H control surface for cavity flow application 23

Figure 3.1 Experimental rig of M219 cavity model (dimensions in meters, adapted from Nayyar (2005) [4]) 28

Figure 3.2 Locations of pressure tabs at the M219 test cavity baseline [4] . . 28

Figure 3.3 Sample computational domain for M219 geometry 29

Figure 3.4 Results of URANS turbulence models for grid convergence study ($M = 0.85$, 2^{nd} order scheme, $\Delta t = 2 \times 10^{-5}$ s) 31

Figure 3.5 FFT obtained RMS pressure at $x/L = 0.95$ in comparison to Rossiter modes and experimental data ($M = 0.85$, 2^{nd} order scheme, $\Delta t = 2 \times 10^{-5}$ s) 32

Figure 3.6 Order of discretization effects on cavity noise prediction via k-ω SST model with experimental data [5] ($M = 0.85$, $\Delta t = 2 \times 10^{-5}$ s) . . 33

Figure 3.7 Order of discretization effects on cavity noise prediction via RNG k-ϵ model with experimental data [5] ($M = 0.85$, $\Delta t = 2 \times 10^{-5}$ s) 34

Figure 3.8 Alternative DES methods predictions to cavity noise levels with experimental data [5] ($M = 0.85$, 3^{rd} order scheme, $\Delta t = 1 \times 10^{-5}$ sec.) 35

Figure 3.9 Results of IDDES method grid convergence study ($M = 0.85$, 3^{rd} order scheme, $\Delta t = 1 \times 10^{-5}$ s) 36

Figure 3.10 Effects of time step on the cavity flow solutions ($M = 0.85$, 3^{rd} order scheme) 37

Figure 3.11 Time-step dependency of IDDES shear layer streamwise mean velocity profiles. The horizontal axis is scaled to $U/U_\infty + x/D$ ($M = 0.85$, 3^{rd} order scheme) 38

Figure 3.12 Turbulence models comparison on cavity flow solutions $M = 0.85$, 3^{rd} order scheme, $\Delta t = 1 \times 10^{-5} s$) 39

Figure 4.1 Instantaneous Mach contours at $1/6^{th}$ of period, T (0.00167 s), of the dominant mode (at $\sim$ 600 Hz). 42

Figure 4.2 Instantaneous spanwise line integral convolution (LIC) images at offset planes 43

Figure 4.3 Instantaneous streamwise line integral convolution (LIC) images 44

Figure 4.4 OASPL along $y/W = 0$, $y/W = 0.2$, and $y/W = 0.4$ over the front wall, ceiling and aft wall of the cavity 44

Figure 4.5 OASPL over the symmetry plane ($y/W = 0$) of the clean cavity 45

Figure 4.6 Cavity with Generic Store Test Section [6] 46

Figure 4.7 Instantaneous spanwise LIC images for cavity with a generic tangent-ogive store 47

Figure 4.8 Instantaneous streamwise LIC images for cavity with a generic store 48

Figure 4.9 OASPL prediction of cavity-with-store configuration via IDDES model 48

Figure 4.10 Doors at 60°, 90°, and 120°, respectively 49

Figure 4.11 Instantaneous LIC images at $z/D = 0.05$ and $z/D = 0.45$ for cavity doors at 90° 50

Figure 4.12 Instantaneous streamwise LIC images for cavity doors at 90° . . 50

Figure 4.13 Instantaneous spanwise LIC images for cavity doors at 90° . . . 51

Figure 4.14 Acoustic characteristics of 90° doors configuration 52

Figure 4.15 Effects of cavity doors angle on the acoustic characteristics along the cavity ceiling centerline 53

Figure 4.16 Instantaneous LIC images at $z/D = 0.05$ and $z/D = 0.45$ for cavity doors at 60° 54

Figure 4.17 Instantaneous spanwise LIC images for cavity doors at 60° . . . 55

Figure 4.18 Instantaneous streamwise LIC images for cavity doors at 60° . . 55

Figure 4.19 Instantaneous spanwise LIC images for cavity doors at 120° . . . 56

Figure 4.20 Instantaneous streamwise LIC images for cavity doors at 120° . . 57

Figure 4.21 Instantaneous LIC images at $z/D = 0.05$ and $z/D = 0.45$ for cavity doors at $120°$ 57

Figure 4.22 Reynolds number effect on transonic open cavity flows ($M = 0.85$) 59

Figure 4.23 Noise prediction at $15 \times L$ distance from the cavity trailing edge centerline via FW-H acoustic analogy method 60

Figure C.1 Hanning window with 0.5 overlap 75

YÖK watermark

LIST OF ABBREVIATIONS

B/L	Boundary Layer
CFD	Computational Fluid Dynamics
DDES	Delayed Detached Eddy Simulation
DES	Detached Eddy Simulation
DNS	Direct Numerical Simulation
f	Frequency, Hz
FFT	Fast Fourier Transform
FW-H	Ffowcs Williams-Hawkings
GIS	Grid-Induced Separation
IDDES	Improved Delayed Detached Eddy Simulation
LES	Large Eddy Simulation
OASPL	Overall Sound Pressure Level
SPL	Sound Pressure Level
SST	Shear Stress Transport
St	Strouhal Number
URANS	Unsteady Reynolds-Averaged Navier-Stokes

CHAPTER 1

INTRODUCTION

1.1 Description of the Problem

In transonic and supersonic regimes, compressible flow past cavities induces complex unsteady aerodynamic characteristics such as:

- Flow separation in the cavity leading edge,
- Shear layer instabilities,
- Vortex shedding,
- Shock wave / boundary layer interactions,
- Self-sustained flow oscillations within the cavity.

Flow past a cavity provokes self-sustained oscillations in the cavity, which can be in longitudinal, transverse, or lateral directions. Depending on the cavity geometric parameters as length, width and depth, these directional oscillations dominate the cavity flow. For instance, if the length is much larger than the depth, longitudinal modes will dominate the flow, whose mechanism is based on Kelvin-Helmholtz instabilities in the shear layer that emanate from the cavity leading edge and grow as they propagate downstream. When the downstream propagating shear layer impinges on the rear wall of the cavity, acoustic disturbances are triggered due to high unsteadiness and instabilities in the shear layer. Acoustic disturbances propagate upstream inside the cavity in the form of pressure waves. When these acoustic disturbances reach the upstream wall of the cavity, they excite the shear layer and form a feedback loop, as illustrated in Fig. 1.1.

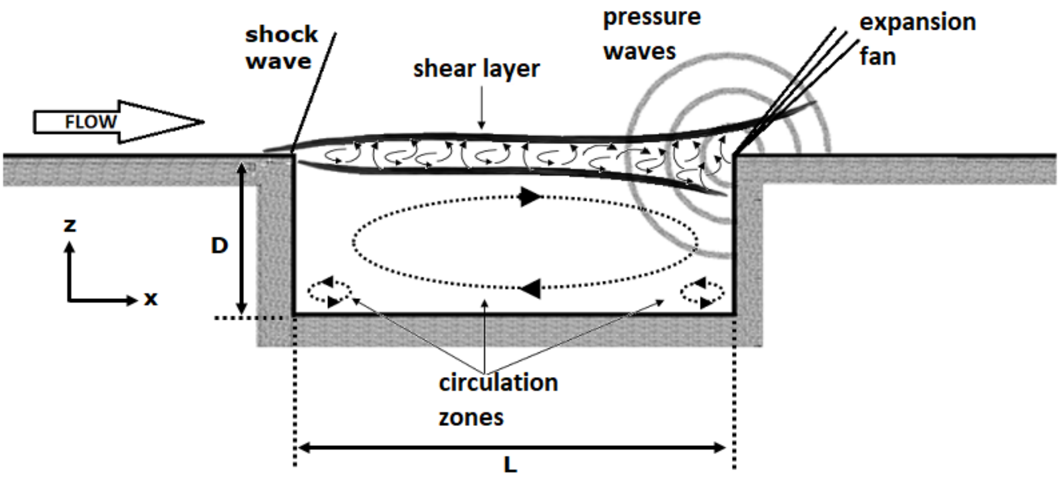

Figure 1.1: Acoustic feedback loop within the cavity

In other words, the feedback mechanism developed inside the cavity is the reinforcement between the instabilities in the shear layer and the pressure waves generated in the cavity due to flow impingement at the aft wall of the cavity.
Acoustic tones formed inside the cavity occur at discrete frequencies corresponding to characteristic pressure patterns in the cavity. Although there is no exact method to determine these modes, there are semi-empirical methods in the literature, given in more detail in the subsequent sections.

1.1.1 Cavity Flow Types

Cavity flow types are classified based on geometric dimensions and the flow conditions. Dominant geometric factors on the cavity flow classification are characteristic Length (L), Depth (D), Width (W). A basic classification of cavity flows is as follows:

- Open (Deep) cavity flow : $L/D < 10$
- Closed (Shallow) cavity flow : $L/D > 13$
- Transitional cavity flow : $10 < L/D < 13$

Flow field characteristics and pressure coefficient, C_p, distributions along the cavity ceiling for cavity flow types are illustrated in Fig. 1.2.

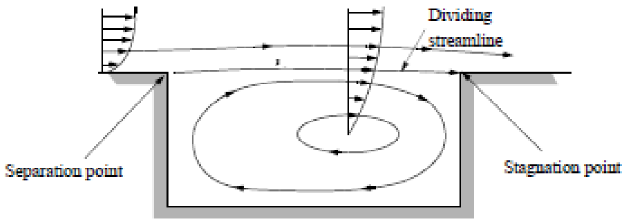
Dividing streamline
Separation point
Stagnation point

(a) Open cavity flow.

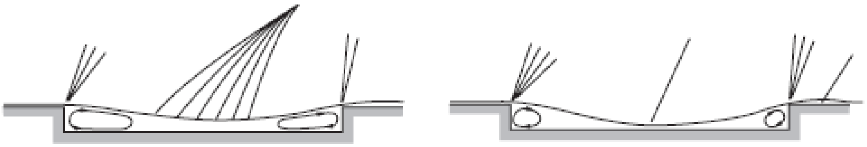

(b) Transitional-open cavity flow. (c) Transitional-closed cavity flow.

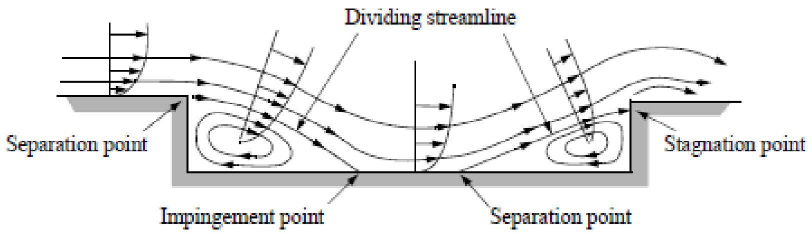
Dividing streamline
Separation point
Stagnation point
Impingement point
Separation point

(d) Closed cavity flow.

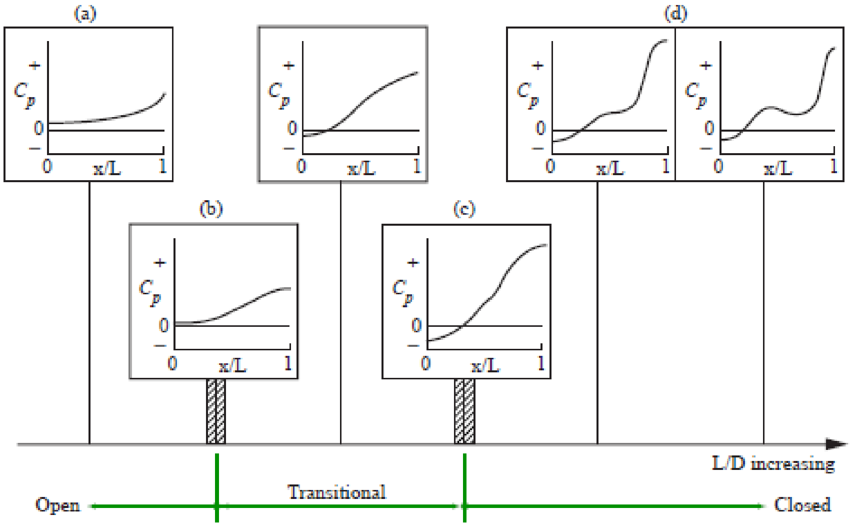

Figure 1.2: Cavity flow type characterization based on cavity baseline pressure distributions [1]

1.1.1.1 Closed Cavity Flows

In closed cavity flows, shear layer separates from the cavity leading edge and re-attaches at the cavity baseline, detaches further downstream and re-attaches at the cavity rear wall, around the trailing edge. These separations and re-attachments cause the formation of two circulation regions inside the cavity, one is around the upstream corner of the cavity and the other is near the downstream corner, as shown in Fig. 1.2. Flow penetration into the cavity increases the local flow speed inside the cavity due to free stream incursion. High speed freestream flow penetrating into the cavity disrupts the upstream propagating pressure waves in the cavity and suppresses the modes. Therefore, closed cavity flow results in non-modal pressure spectrum, as in Fig. 1.3.

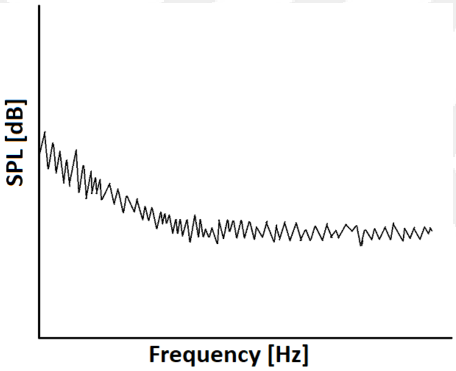

Figure 1.3: Typical acoustic spectrum in closed cavity flows.

Despite their non-modal spectrum, closed cavities are not preferred in weapons bays because of the adverse static pressure gradient characteristics that can create nose-up pitching moment on internal stores as shown in Fig. 1.4.

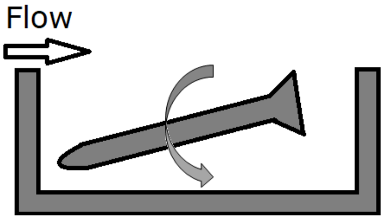

Figure 1.4: Nose-up pitching moment induced closed cavity flow on a store in the cavity.

1.1.1.2 Open Cavity Flows

Open cavity flows are encountered in relatively short and deep cavities where the detached shear layer creates a passage over the cavity length rather than penetrating into the cavity, and re-attaches at the cavity rear wall, Fig. 1.2. This process results in the formation of unsteady pressure waves from the rear wall re-attachment region, which propagate upstream in the cavity and interact with the detached shear layer. As a result of this, the boundary of the shear layer oscillate. Hence, a feedback mechanism is formed within the cavity. This feedback loop is identified as the source of unsteady pressure spectra with high modal Sound Pressure Levels (SPL) associated with open type cavity flows.

Unlike the closed cavity flow, open cavity flow has rather smooth pressure coefficient, C_p, distribution near the cavity baseline. In other words, open cavity flow has much lower C_p gradient along the cavity and lower maximum C_p value near the rear wall of the cavity, which directly affects the separation characteristics, Fig. 1.2. Therefore, open cavities are usually preferred in the design of internal weapon bays.

Despite favorable separation characteristics of open cavity flows, they exhibit modal pressure spectra with high intensity modal peaks, Fig. 1.5. These modal peaks can damage both the aircraft structures and the stores carried in the weapon bay. Possible damage of modal peaks to the aircraft and/or stores brings the requirement to use acoustic suppression devices to control the flow in the cavity and therefore to suppress the damaging modal peaks.

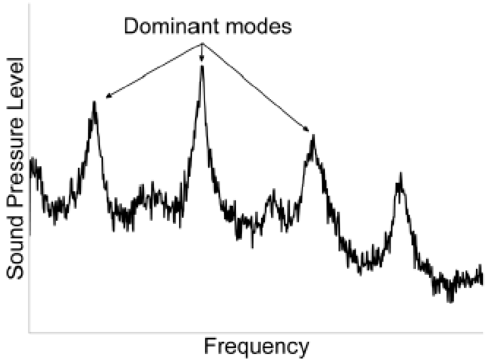

Figure 1.5: Typical modal spectrum of open cavity flows.

1.1.1.3 Transitional Cavity Flows

Transitional cavity flows are encountered in the transition region from open cavity to closed cavity. As L/D ratio starts to increase, cavity flow characteristics are set out to switch from open cavity flow characteristics to closed ones. In this sense, modal spectrum and rather smooth pressure coefficient distribution of open cavity flow evolves to non-modal pressure spectrum and high gradients in the C_p distribution, Fig. 1.2, which are the characteristics of closed cavity flows.

Transitional cavity flows consist of transitional open flow and transitional closed flow. When L/D ratio is close to the boundary of closed flow but still in transitional regime, it is called transitional closed cavity flow and otherwise, transitional open cavity flow. The boundaries for transitional open or closed flow are not precise and depend on the flow conditions.

In transitional closed flows, characteristics of closed cavity flow are dominant and the flow exhibits large longitudinal pressure gradients, Fig. 1.2. As in the closed cavity flow, large pitching moments may be imposed on any store carried in the cavity, causing nose-up pitching moment on the store. Transitional open flows, on the other hand, behave largely like open cavity flows. Transitional open cavity flows have larger pressure gradients than open cavity flows that impose pitching moments on existent stores in the cavity, though it is not as severe as for closed cavity flows. Also, transitional open flows have modal characteristics similar to open flows.

1.2 Literature Search

In previous research on transonic cavity flow simulations, scale resolving turbulence models such as Large Eddy Simulation (LES) and Detached Eddy Simulation (DES) are preferred to predict the turbulent cavity flow and resulting noise. These methods basically rely on resolving turbulent scales of the complex cavity flow rather than using statistical modelling [7], because the small scale eddies present in the unsteady shear layer have a critical effect on the generation of acoustic waves. In LES, significantly lower portion of the flow is modelled compared to Unsteady Reynolds-

Averaged Navier-Stokes (URANS) methods, which proves the accuracy of the LES. However, computational cost of LES is hard to afford for high Reynolds number flows [4, 8].

DES is a hybrid method which is developed to take advantages of URANS methods within the boundary layer region and LES in regions outside the boundary layer. Advantage of DES methods over the LES methods is computational efficiency because of employing URANS methods in the wall regions [4, 8–10].

URANS methods, on contrary to LES method, use fully statistical models rather than scale resolving. This brings the drawback of decreased accuracy in cavity solutions. However, URANS methods are not a complete scratch but they have a level of accuracy in prediction of cavity noise. This proposes to determine the availability of URANS methods for cavity configurations.

In the present study, URANS methods are utilized alongside with DES methods to draw the borders of URANS methods in cavity flow solutions. Applicability of URANS methods to various cavity configurations (clean cavity, cavity with a store and cavity with doors) is investigated to determine the suitability and model requirements for the current problem. Being a powerful method, DES is also employed with different variants to ascertain the limits of the models in cavity flow solutions.

1.3 The Objectives of The Thesis

The objectives of the thesis are:

- To assess the applicability and limitations of turbulence models available in ANSYS/Fluent commercial CFD tool solver to cavity flow solutions,
- To identify the requirements of turbulence models in cavity flow predictions,
- To compare cavity acoustic predictions of turbulence modeling techniques,
- To revise the effects of internal stores and doors on cavity acoustics,
- To produce farfield noise characteristics of cavity flows via in-house Fortran code.

1.4 The Scope of The Thesis

The main focus of this work is to determine applicability and level of accuracy of existing turbulence models to turbulence and noise predictions of cavity flows. Turbulence modeling (URANS variants) and hybrid turbulence solution methods (DES variants) that synthesize modeling and scale resolving techniques in the solution of turbulent flows are utilized. Effects of grid resolution, order of numerical scheme and computational time step are covered. Reynolds number effect on the cavity flows is also identified.

After the assessment of the most suitable turbulence model for clean cavity flows (no doors, stores and etc.), how internal geometries affect the flow and acoustic characteristics of the cavity flows are identified. These internal geometries include an internal store and cavity doors. Farfield noise characteristics are also be computed.

This work identifies the limits of turbulence models in cavity turbulent flow and noise predictions, acoustic characteristics of clean cavity, cavity a generic store and cavity with doors. Outcomes of this thesis can be used in all similar cavity analyses.

CHAPTER 2

GOVERNING EQUATIONS OF FLUID DYNAMICS AND NUMERICAL METHODS

2.1 Navier-Stokes Equations

Navier-Stokes (N-S) equations are the governing equations of fluid dynamics, which cover the conservation of mass and conservation of momentum. N-S equations in the absence of source terms, body and buoyant forces along with the conservation of energy equation are given in Eqn. 2.1.1 in Cartesian coordinates. Navier-Stokes equations, in their most general form, cover the compressible, time dependent and viscous fluid dynamics for Newtonian fluids. Cavity flow in transonic speeds is composed of time dependent, compressible and viscous flow physics. Therefore, governing Navier-Stokes equations are considered in their most general form, without any source term in the solution domain for the current problem.

$$
\begin{aligned}
\frac{\partial \rho}{\partial t} + \frac{\partial}{\partial x_i}(\rho u_i) &= 0 \\
\frac{\partial}{\partial t}(\rho u_i) + \frac{\partial}{\partial x_j}(\rho u_j u_i) &= -\frac{\partial P}{\partial x_i} + \frac{\partial \tau_{ij}}{\partial x_j} \\
\frac{\partial}{\partial t}(\rho E) + \frac{\partial}{\partial x_j}(\rho u_j H) &= \frac{\partial}{\partial x_j}(u_i \tau_{ij}) + \frac{\partial}{\partial x_j}\left(k \frac{\partial T}{\partial x_j}\right)
\end{aligned}
\tag{2.1.1}
$$

where u_i is the velocity vector with $\vec{u} = [u, v, w]^T$ and x_i is the coordinates vector with $\vec{x} = [x, y, z]^T$, and t denotes time, P denotes pressure and ρ denotes density, respectively. τ_{ij} in the conservation of momentum equation is the viscous stress tensor defined as:

$$
\tau_{ij} = 2\mu S_{ij} + \lambda \frac{\partial u_k}{\partial x_k}\delta_{ij} = 2\mu S_{ij} - \left(\frac{2\mu}{3}\right)\frac{\partial u_k}{\partial x_k}\delta_{ij}
\tag{2.1.2}
$$

where $\lambda + \frac{2}{3}\mu = 0$ by Stoke's hypothesis for the bulk viscosity, μ is the dynamic viscosity coefficient, λ is the second viscosity coefficient and S_{ij} is the strain rate tensor given by:

$$S_{ij} = \frac{1}{2}\left(\frac{\partial u_i}{\partial x_j} + \frac{\partial u_j}{\partial x_i}\right) \tag{2.1.3}$$

In the conservation of energy equation, T is the temperature, E is the total energy, H is the total enthalpy and k is the thermal conductivity. Total energy and total enthalpy are given as:

$$E = e + \frac{1}{2}u_i u_i \quad H = h + \frac{1}{2}u_i u_i \tag{2.1.4}$$

where e is the internal energy and h is the enthalpy in Eq.2.1.4.

2.2 Turbulence Modelling

In engineering applications, most of the fluid flows have turbulent flow characteristics. A flow being laminar or turbulent is determined by the relative importance of inertial and viscous forces present in a fluid motion. Reynolds number (Re) is the parameter that determines the relative importance of inertial and viscous forces, given by:

$$\mathrm{Re}_L = \frac{\text{Inertial Forces}}{\text{Viscous Forces}} = \frac{\rho V L}{\mu} \tag{2.2.1}$$

where ρ is the air density, V is flow velocity, L is characteristic length and μ is the dynamic viscosity of air. If the viscous forces are dominant (i.e. low Re), flow is laminar. If the inertial forces are much larger than viscous forces, (i.e. high Re), the flow is turbulent. High Re flows are usually a result of high speed flows. In aerospace applications, almost all the air flows are turbulent, which is also the case in cavity flows. Turbulent flows are characterized by irregular, chaotic, diffusive, rotational and dissipative nature of fluid particles. Turbulence is not a completely stochastic phenomenon [3]. Turbulent flows are also highly rotational flows that are composed of various sizes of eddies, whose formation takes the large proportion of the flow energy. This energy is transferred from larger eddies to the smaller eddies present in the turbulent flow. This energy transfer process is called energy cascade. As a result of the energy cascade, eddy energy in the flow is eventually transformed to heat by dissipation.

Turbulence is the unsolved problem of fluid dynamics. There is no precise or commonly-agreed way to solve the turbulence in fluid flows. However, there are models and techniques developed for turbulent flow solutions, some of which are completely based on statistical modeling like URANS models, while some intend to solve the turbulent scales in the flow that could be all the turbulent scales (DNS) or a proportion (DES, LES). Fig. 2.1 compares the turbulence models both in resolved/modeled flow physics and computational cost of each model.

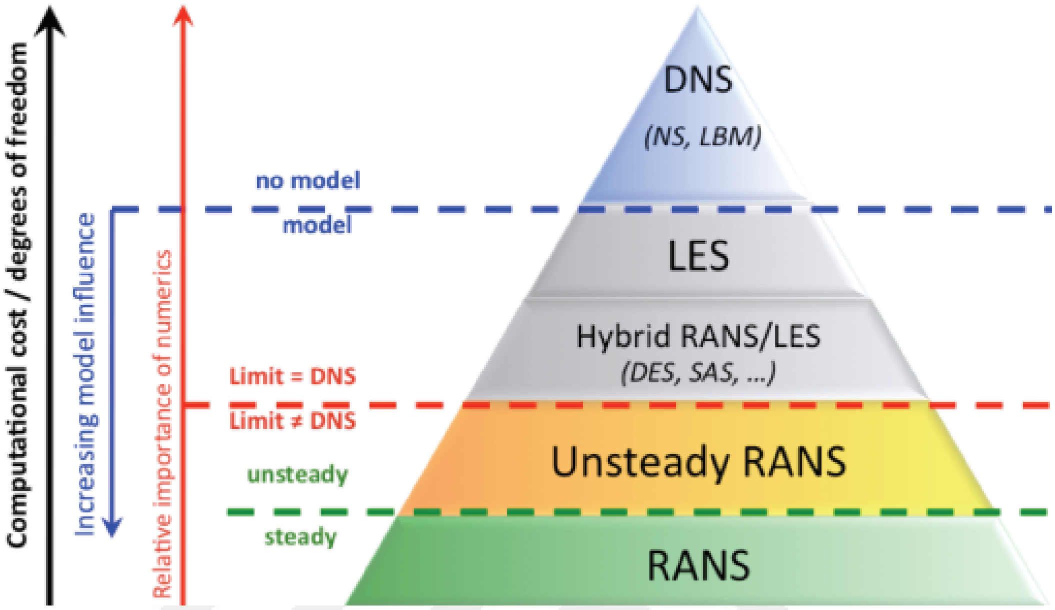
Computational cost / degrees of freedom
Increasing model influence
Relative importance of numerics
no model
model
Limit = DNS
Limit ≠ DNS
unsteady
steady
DNS
(NS, LBM)
LES
Hybrid RANS/LES
(DES, SAS, ...)
Unsteady RANS
RANS

Figure 2.1: Turbulence models classification [2]

RANS models are completely based on modeling the flow physics while DNS resolves entire flow physics. RANS models are basically based on statistical models basically, which model all the flow physics. Although modeling nature provides RANS models relatively low computational costs, the uncertainty due to modeling the entire flow physics is a severe drawback of the model.

DNS aims to resolve all the scales present in the flow down to viscous dissipation scale by eliminating modeling beyond N-S equations. DNS has strict restrictions on computational grid both in time, Δt, and space, Δx, to resolve all the scales in full. This results in dramatically increased computational cost, especially for high Reynolds number flows. Grid requirement of DNS method is challenging to meet with available resources. Hence, DNS is not feasible currently for high Re flows.

2.2.1 Resolution Requirements

Turbulent flows compose of various ranges of length and time scales. The largest scales in a turbulent flow are referred as integral length scales, denoted by L, which are the sizes of the largest eddies that are responsible for most of the energy and momentum transport. Integral length scales depend on the physical domain of the flow. The smallest hydrodynamic scales in a turbulent flow are referred as Kolmogorov scales, denoted by η, whose sizes are determined by the viscosity. Energy cascade takes place from larger scales to smaller scales present in the turbulent flow. As the size of length scale decreases and approaches to Kolmogorov scales, the effect of viscosity increases and dissipation becomes important, which causes the transformation of kinetic energy to heat by energy dissipation.

Turbulence models have distinct approaches to resolution of turbulent length scales. For instance, DNS aims to resolve Kolmogorov scales while RANS has no concern on resolution of eddies due to its modeling nature. Piomelli [3] provides the grid resolution requirements of DNS, LES and RANS models, as shown in Fig. 2.2. Approximated computational costs of DNS and LES models are further discussed in App. A.

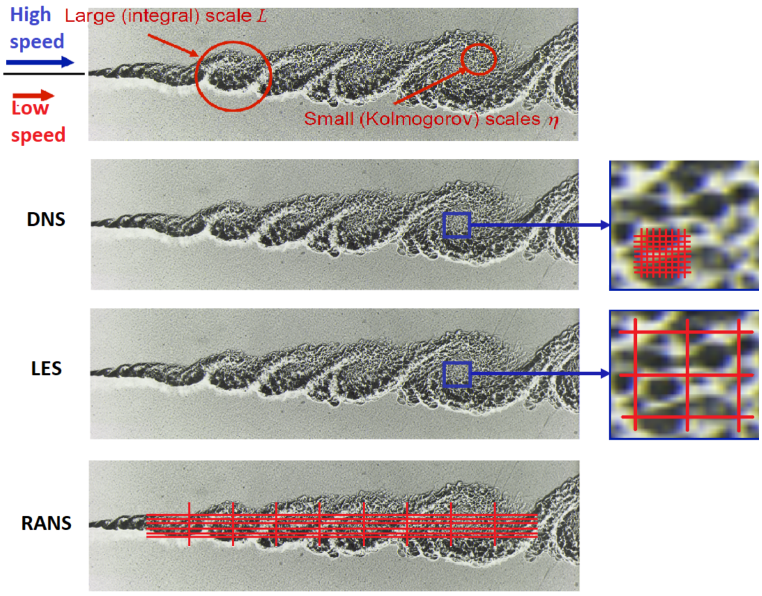

Figure 2.2: Resolution requirements of DNS, LES, and RANS (modified from Piomelli [3])

2.2.2 Large Eddy Simulation (LES)

Large Eddy Simulation (LES) is a method that fits in between DNS and RANS methods in terms of both computational cost and order of accuracy as illustrated in Fig. 2.1. The idea behind LES is to resolve the energy carrying large eddies present in the flow, while smaller sub-grid scale structures are modeled. Since the large and the smaller eddies are in continuous interaction and energy cascade takes place from the larger eddies toward the smaller ones, the effect of the small scales must be taken into account, which are modeled in LES. Main difference of LES method from DNS is the modeling of the small-scale turbulent structures. On the contrary to RANS models, which model all the flow, LES only models small scales, which increases the order of accuracy of LES. Since the smallest scales in a turbulent flow are assumed to be isotropic and universal [3, 11], modeling of these small scales does not have significant adverse effects on the total flow physics. Currently unaffordable computational costs of DNS directed research to alternative methods with improved simulation of flow physics such as LES. Although computational requirements of LES method are more affordable compared to DNS, LES is still expensive for high Reynolds number flows.

2.2.3 Unsteady Reynolds-Averaged Navier-Stokes (URANS) Modelling

Reynolds-Averaged Navier-Stokes (RANS) models provide economic and suitable approach for most of complex engineering problems with a certain level of accuracy. Although RANS models come with a level of accuracy, none of the models are limitless. Some models may serve with a better accuracy for a specific problem. Therefore, the most suitable URANS model needs to be explored for the problem of interest.

2.2.3.1 Reynolds Decomposition

RANS models based on statistical modeling of turbulent parameters separate the flow paramters into time-averaged and instantaneous components. This is achieved through Reynolds decomposition, which is mainly based on the assumption of turbulence field being statistically steady with time averaging over turbulent quantities. In Reynolds decomposition, turbulent flow quantities are decomposed into two parts; average and fluctuating components, as shown in Fig 2.3.

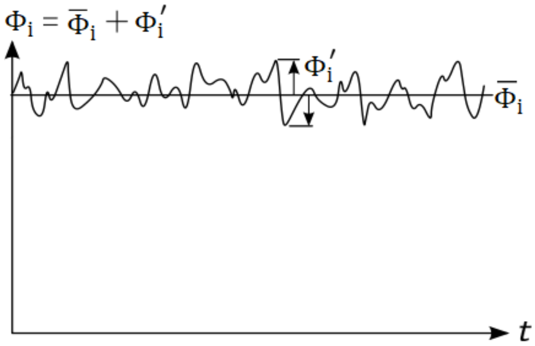

Figure 2.3: Reynolds decomposition of turbulent quantities

A turbulent quantity (such as the velocity), ϕ, is expressed as:

$$\phi = \bar{\phi} + \phi^{`} \tag{2.2.2}$$

where $\bar{\phi}$ is the time averaged value and $\phi^{`}$ is the instantaneous fluctuation. Time averaged quantities are expressed as:

$$\bar{\phi} = \frac{1}{T}\int_0^T \phi(t)dt \tag{2.2.3}$$

2.2.3.2 URANS Equations

When turbulent quantities with Reynolds decomposition are substituted into N-S equations in Eq. 2.1.1, URANS equations are obtained as:

$$\begin{gathered}
\frac{\partial\bar{\rho}}{\partial t} + \frac{\partial(\bar{\rho}\widetilde{u_j})}{\partial x_j} = 0 \\
\frac{\partial(\bar{\rho}\widetilde{u_i})}{\partial t} + \frac{\partial(\bar{\rho}\widetilde{u_i}\widetilde{u_j})}{\partial x_j} = -\frac{\partial P}{\partial x_i} + \frac{\partial\overline{\sigma_{ij}}}{\partial x_j} - \frac{\partial R_{ij}}{\partial x_j} \\
\frac{\partial(\bar{\rho}\widetilde{E})}{\partial t} + \frac{\partial(\bar{u_j}\bar{\rho}\widetilde{H})}{\partial x_j} = \frac{\partial(\overline{u_i\sigma_{ij}})}{\partial x_j} - \frac{\partial\overline{q_j}}{\partial x_j} - \frac{\partial\overline{Q_j}}{\partial x_j}
\end{gathered} \tag{2.2.4}$$

where $\overline{\sigma_{ij}}$ is the viscous stress tensor and R_{ij} is the Reynolds stress tensor, which are given in App. B.1.

2.2.3.2.1 k-ω Shear Stress Transport (SST) Two-Equation Model

k-ω SST turbulence model is a two-equation eddy-viscosity model proposed by Menter (1994) [12]. The k-ω SST model combines the best aspects of already existing k-ϵ and k-ω models to reveal a superior two-equation model. In k-ω SST model, a blending function, F_1, is used to activate Wilcox's k-ω model in near-wall regions and k-ϵ model far from solid walls and in free stream region [12, 13]. Shear stress transport in k-ω SST model improves suitability of Wilcox's k-ω model to flows with strong adverse pressure gradients by modifying the eddy viscosity within boundary layers. The achievement of the model comes from taking the shear stress transport into account, which was deficient in previous two-equation models. Johnson (1985) [14] showed that modeled shear stress transport proportional to turbulent kinetic energy significantly improves the results. k-ω SST model equations are given in Eq. 2.2.5 and 2.2.6.

$$\frac{\partial}{\partial t}(\rho k) + \frac{\partial}{\partial x_j}(\rho u_j k) = \tau_{ij}\frac{\partial u_i}{\partial x_j} - \beta^* \rho \omega k + \frac{\partial}{\partial x_j}\left((\mu + \sigma_k \mu_t)\frac{\partial k}{\partial x_j}\right) \tag{2.2.5}$$

$$\begin{aligned}\frac{\partial}{\partial t}(\rho \omega) + \frac{\partial}{\partial x_j}(\rho u_j \omega) = \frac{\gamma}{\nu_t}\tau_{ij}\frac{\partial u_i}{\partial x_j} - \beta \rho \omega^2 + \frac{\partial}{\partial x_j}\left((\mu + \sigma_\omega \mu_t)\frac{\partial \omega}{\partial x_j}\right) \\ +2(1 - F_1)\frac{\rho \sigma_{\omega 2}}{\omega}\frac{\partial k}{\partial x_j}\frac{\partial \omega}{\partial x_j}\end{aligned} \tag{2.2.6}$$

where k is the turbulent kinetic energy and ω is the specific dissipation rate.

2.2.3.2.2 RNG k-ϵ Two-Equation Model

RNG k-ϵ model is based on a statistical re-normalization group (RNG) theory. RNG theory provides standart k-ϵ model extra refinements, which provide an increased accuracy in rapidly strained and swirling flow solutions such as backward facing step and cavity flows. RNG theory also provides an analytical method for the computation of effective viscosity that accounts for low Reynolds-number flows, unlike the standard k-ϵ model. RNG k-ϵ model equations are given in Eq. 2.2.7 and 2.2.8.

$$\frac{\partial}{\partial t}(\rho k) + \frac{\partial}{\partial x_i}(\rho u_i k) = \frac{\partial}{\partial x_j}\left(\alpha_k \mu_{\text{eff}}\frac{\partial k}{\partial x_j}\right) + G_k + \rho \epsilon - Y_m + S_k \tag{2.2.7}$$

$$\frac{\partial}{\partial t}(\rho \epsilon) + \frac{\partial}{\partial x_i}(\rho u_i \epsilon) = \frac{\partial}{\partial x_j}\left(\alpha_\epsilon \mu_{\text{eff}}\frac{\partial \epsilon}{\partial x_j}\right) + C_{1\epsilon}\frac{\epsilon}{k}G_k - C_{2\epsilon}\rho\frac{\epsilon^2}{k} - R_\epsilon + S_\epsilon \tag{2.2.8}$$

where G_k is the turbulent kinetic energy, k is the generation term due to mean velocity gradients and Y_m accounts for the fluctuation dilatation in compressible turbulence to the overall dissipation rate. α_k and α_ϵ are inverse effective Prandtl numbers, and S_k and S_ϵ are user-defined source terms in k and ϵ equations, respectively.

2.2.4 Detached Eddy Simulation (DES)

2.2.4.1 Classical Detached Eddy Simulation (DES)

Difficulties in near wall modeling and high computational costs of LES model and inadequate flow physics in RANS methods, because of its modeling nature, has lead to combinations of URANS and LES methods in turbulence solutions. DES is a particular class of hybrid RANS/LES techniques which attempts to agglomerate the best aspects of RANS and LES methods. Classical DES is originally a modified version of Spalart-Almaras (S-A) one-equation model which employs RANS equations in attached boundary layers and LES method anywhere else.

The original Spalart-Almaras (S-A) one-equation model is given by:

$$\begin{aligned}\frac{\partial \widetilde{\nu}}{\partial t} + u_j \frac{\partial \widetilde{\nu}}{\partial x_j} &= c_{b1}(1 - f_{t2})\widetilde{S}\widetilde{\nu} - \left[c_{w1} f_w - \frac{c_{b1}}{\kappa^2} f_{t2}\right] \left(\frac{\widetilde{\nu}}{d}\right)^2 \\ &+ \frac{1}{\sigma}\left[\frac{\partial}{\partial x_j}\left((\nu + \widetilde{\nu})\frac{\partial \widetilde{\nu}}{\partial x_j}\right) + c_{b2}\frac{\partial \widetilde{\nu}}{x_i}\frac{\partial \widetilde{\nu}}{x_i}\right]\end{aligned} \tag{2.2.9}$$

Further details for S-A model are given in Appendix B.5.
DES model uses a modified wall distance in S-A model, as approximated by:

$$d_{\text{DES}} = \min(d, C_{\text{DES}}\Delta) \tag{2.2.10}$$

where d_{DES} is the modified length scale that guarantees the S-A length scale in near-wall regions for $d << \Delta$ and modifies the local grid spacing for DES requirements away from the walls for $d >> \Delta$. $C_{\text{DES}} = 0.65$ is an empirical DES constant. Δ is the maximum local grid spacing in 3-dimensional space, obtained by;

$$\Delta = \max(\Delta_x, \Delta_y, \Delta_z) \tag{2.2.11}$$

Since DES makes use of RANS and LES methods in combination, it deserves a carefully designed computational grid that satisfies both RANS and LES grid requirements in the regions of interest for each of the models.

2.2.4.2 Issues in DES

Classical DES reveals some issues in the successful implementation of the model, which derived further developments as delayed detached eddy simulation (DDES) and improved delayed detached eddy simulation (IDDES). Main concerns in the DES turbulence models are:

i. Gray area problem
When DES model switches from URANS to LES mode in separated B/L case, there occurs a region where neither RANS nor LES mode is active. DES is designed as the turbulent B/L separates at some point, the flow is expected to be simulated by LES mode in the regions of separation. In the immediately following regions of separation, LES mode is activated to resolve the turbulence unlike RANS in the attached B/L regions. However, the grid structure is not convenient for LES to handle the turbulence. Therefore, when the LES mode is turned on in such zones, a region called ”gray area” in the interface of RANS and LES is generated.

ii. Grid induced separation (GIS)
Model switching mechanism in DES is purely grid sensitive that boundary layer grid and the region just outside the boundary layer where LES mode is activated must be carefully designed. If not, LES mode may be activated inside the attached boundary layer, which gives rise to an early separation of the flow caused by inconvenient switching of LES mode because of the grid resolution.

iii. Logarithmic-layer mismatch (LLM)
Log-layer mismatch is a phenomenon encountered usually in hybrid RANS/LES methods, like DES, that is a result of the inner (modeled) log-layer and outer (resolved) log-layers mismatch. Inner log-layer is modeled by RANS model while outer log-layer is resolved by LES method. The intercepts in the log-layer formulation, i.e. C in $U^+ = log(y+)/\kappa + C$, does not match because of the modeling and resolving approaches on each sides, which is called ”log-layer mismatch” [15]. The log-layer mismatch may cause under-prediction of the skin friction coefficient by approximately 15$\%$ [16, 17].

2.2.4.3 Delayed Detached Eddy Simulation (DDES)

One of the main issues in classical DES method is about handling the ambiguous grids that have wall parallel grid size is in the order of boundary layer thickness, δ. Menter and Kuntz [18] implemented a B/L shield function, r_d, to shield the B/L so that the activation of LES mode in attached boundary layers is prohibited. The method is called as delayed DES (DDES) because of delaying the activation of LES within attached B/L's. Therefore, DDES cures the GIS issued in classical DES. The shield function of DDES model is given as:

$$r_d = \frac{\widetilde{\nu}}{\sqrt{U_{i,j}U_{i,j}}\kappa^2 d^2}; \quad \kappa = 0.41 \tag{2.2.12}$$

where $\widetilde{\nu}$ is the kinematic viscosity, $U_{i,j}$ is the velocity tensor, κ is the Karman constant, and d is the wall distance in B/L. Similar to one-equation S-A model, $r_d = 1$ in the log-layer and it decreases gradually to zero at the outer edge of the B/L [15, 19]. The shielding function acts in:

$$f_d = 1 - \tanh([8r_d]^3) \tag{2.2.13}$$

where $f_d = 1$ in LES region and 0 elsewhere. f_d relation employs a hyperbolic blending function, tanh, to provide a smooth transition from LES region to URANS region.

DDES is proposed by a modification to one equation S-A model length scale, d, by:

$$\widetilde{d} \equiv d - f_d \max(0, d - C_{\text{DES}}\Delta) \tag{2.2.14}$$

$f_d = 0$ (RANS region) yields $\widetilde{d} = d$ and $f_d = 1$ (LES region) yields $\widetilde{d} = \min(d, C_{\text{DES}}\Delta)$, which is the classical DES model.

Although DDES method showed a success in curing the ambiguous grid issue and increased the robustness of classical DES, log-layer mismatch issue is still existent in DDES model.

2.2.4.4 Improved-Delayed Detached Eddy Simulation (IDDES)

Log-layer mismatch (LLM) is common to both DES and DDES hybrid RANS/LES methods because of RANS modeling of the inner log-layer and LES resolving the outer log-layer. As discussed in issues encountered in DES, LLM issue causes an error by approximately 15% in the skin friction coefficient. Shur *et al.* [16] proposed a further modification to DDES model that intends to cure the LLM issue. The model is called as Improved DDES (IDDES). The word improved implies improved wall modeling capability of the model. The major difference of IDDES model from DDES method is that it employs both DDES and Wall Modeled LES (WMLES) depending on the inflow (or initial) conditions [16, 18]. That is, activation of DDES or WMLES depends on the inflow containing turbulent content or not. If inflow does contain turbulent content, IDDES turns out to switch to WMLES branch, and DDES branch otherwise.

There are alternatives to turbulent inflow conditions activating the WMLES branch. These alternatives are the results of the geometry of interest, such as backward facing step. Some specific geometries induce unsteadiness in the flow and activate the WMLES branch of IDDES. Since the flow over cavities is very similar to backward facing step, IDDES is considered as one of the most convenient methods for cavity flow simulations [20–22].

IDDES also includes some empirical functions to ensure the correct activation and performance of the sub-branches, i.e. DDES and WMLES. The precedence of the WMLES compared to DES comes from the empirical base improvements to WMLES model that provide a significant increase in the model capability to resolve near wall regions. Switching between the sub-models is achieved by use of blending functions.

The original proposal of IDDES model by Shur *et al.* [16] is based on S-A one equation RANS model. Gritskevich [23] implemented the model based on k-ω SST model, which is used in the present work.

k-ω SST based IDDES model formulation uses hybrid length scale in the turbulent kinetic energy equation in k-ω SST model as:

$$\frac{\partial(\rho k)}{\partial t} + \frac{\partial(\rho U_i k)}{\partial x_i} = \widetilde{P_k} - \frac{\rho k^{3/2}}{L_{\text{hybrid}}} + \frac{\partial}{\partial x_i}\left[(\mu + \sigma_k \mu_t)\frac{\partial k}{\partial x_i}\right] \tag{2.2.15}$$

where hybrid length scale, L_{hybrid}, is defined as:

$$L_{\text{hybrid}} = L_{\text{IDDES}} = \widetilde{f}_d(1 + f_e) \times L_{\text{RANS}} + (1 - \widetilde{f}_d) \times L_{\text{LES}} \tag{2.2.16}$$

with L_{IDDES} being the IDDES length scale and L_{LES} is the LES length scale. $\widetilde{f}_d$ is:

$$\widetilde{f}_d = \max[(1 - f_{dt}), f_B] \tag{2.2.17}$$

In IDDES model, sub-grid length scales are not only dependent on the grid spacing but also on the wall distance, which provides further sensitivity to the model through $\widetilde{f}_d$. It is a function of both geometry, f_B, and the flow, f_{dt}.

If $f_e > 0$ and $f_B = 0$, IDDES model functions in the WMLES mode:

$$L_{\text{hybrid}} = L_{\text{IDDES}} = f_B(1 + f_e) \times L_{\text{RANS}} + (1 - f_B) \times L_{\text{LES}} \tag{2.2.18}$$

The refined grid scale in IDDES reads:

$$\Delta = \min[\max(C_W \Delta_{\text{max}}, C_W d, \Delta_{\text{min}}), \Delta_{\text{max}}] \tag{2.2.19}$$

where $C_W = 0.15$, and d is the distance to the wall. The minimum and maximum grid scales, Δ_{min} and Δ_{max}, are given as:

$$\Delta_{\text{min}} = \min(\Delta_x, \Delta_y, \Delta_z) \quad \Delta_{\text{max}} = \max(\Delta_x, \Delta_y, \Delta_z) \tag{2.2.20}$$

2.3 Acoustics

2.3.1 Ffowcs Williams – Hawkings (FWH) Acoustic Analogy

Farfield noise prediction is of common interest in the computational aeroacoustics (CAA) community. It is possible to compute aerodynamic noise at an observer location by CFD solutions of unsteady flow phenomena in the field of interest, which covers both the aerodynamic noise source(s) and the observer in the computational domain. However, as the distance of the observer to the noise source gets larger and larger, computational cost of CFD gets unaffordable. Therefore, the research focused on coupling the CFD with acoustic analogy methods for the computations of far-field noise generation and propagation of aerodynamic noise. In this respect, Ffowcs Williams and Hawkings (1969) [24] proposed an acoustic analogy method for the computation of aerodynamically generated noise propagation to the far field through inhomogeneous wave equation [24]. FW-H method accounts for the presence of a solid body in the flow field that moves in an arbitrary speed. The model consists of two surface sources (monopole and dipole sources) and a volume source (quadruple source) in the formulation where all of these sources are independent.

FW-H formulation takes advantage of the simple acoustic sources that are monopole, dipole and quadruple sources. Monopole sources generate the thickness noise, which is directly dependent on the body (airfoil, blade etc.) geometric properties in the flow field. Monopole sources radiate acoustic waves in all directions. Dipole sources are responsible for the loading noise. A dipole source is a combination of two monopole sources with equal strengths and opposite phases. Monopole and dipole sources are surface sources and results of linearized aerodynamics. Quadruple acoustic source, on the other hand, is composed of two dipoles (or four monopoles) that may be arranged in different strengths and phases. Quadruple sources take into account the nonlinear effects, i.e. nonlinear wave propagation, local speed of sound variation, shock noise, and noise generated by turbulence, vorticity etc. [25]. Quadruple noise is critical especially at high speeds.

Since the cavity flow of interest operates in transonic speeds, all of monopole, dipole and quadrupole noise sources have significant effects on the radiated farfield noise. Therefore, all are taken into account in cavity flow farfield noise predictions.

In FW-H acoustic analogy, sound sources are enclosed by a control surface that is represented by $f(x,t) = 0$, mathematically, as shown in Fig. 2.4. In CFD and acoustic analogy coupling, N-S equations are solved in the computational domain for nonlinear effects and unsteady flow variable data is collected on the control surface. Then, it is linearly propagated to any observer location by FW-H acoustic analogy method [26]. An in-house FW-H acoustic analogy Fortran program is utilized in calculation of farfield noise.

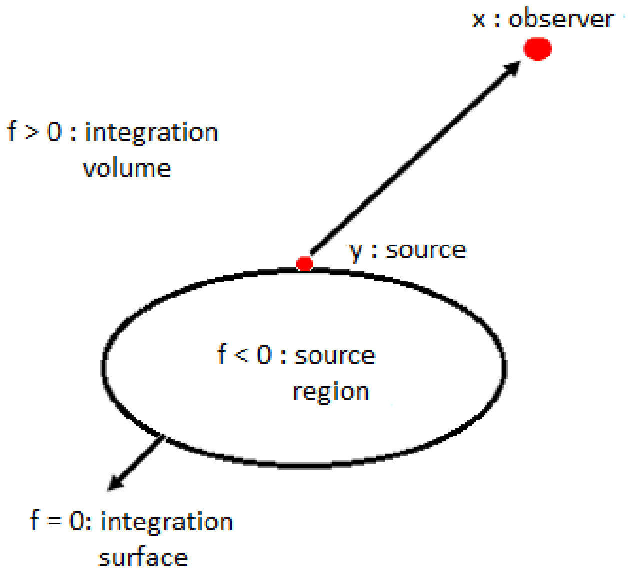

Figure 2.4: FW-H control surface definition

FW-H model reads:

$$4\pi p'(\vec{x},t) = \int_{f=0} \left[\frac{\rho_0(\dot{U}_n + U_{\dot{n}})}{r(1-M_r)^2} + \frac{\rho_0 U_n (r\dot{M}_r + c_0 M_r - c_0 M^2)}{r^2(1-M_r)^3} \right]_{ret} dS$$

$$+ \frac{1}{c_0} \int_{f=0} \left[\frac{\dot{L}_r}{r(1-M_r)^2} + \frac{L_r (r\dot{M}_r + c_0 M_r - c_0 M^2)}{r^2(1-M_r)^3} \right]_{ret} dS \qquad (2.3.1)$$

$$+ \int_{f=0} \left[\frac{L_r - L_M}{r(1-M_r)^2} \right]_{ret} dS$$

where $[\ ]_{ret}$ indicates that source terms are evaluated at retarded time. In Eq. 2.3.1, first term represents thickness noise with $U_i = \rho u_i/\rho_0 + v_i(1-\rho/\rho_0)$. Second and third terms stand for the loading noise with $L_i = P_{ij} n_j + u_i(u_n - v_n)$ and $P_{ij} = (p - p_0)\delta_{ij} - \sigma_{ij}$ where σ_{ij} is the viscous stress tensor. ρ_0 is the free stream air density, v_i is the surface velocity and M_i is the surface Mach number based on free stream speed of sound, c_0. Parameters with dots are the time derivatives with respect to source time. Subscripts in Eq. 2.3.1 stand for scalar product with either the surface unit normal vector, $\vec{n_i}$, the unit radial vector, $\vec{r_i}$, or the Mach number vector M_i, i.e. $\dot{M}_r = \dot{M}_i r_i$, provided by Farassat Equation 1A [27].

In Eq. 2.3.1, volumetric sources outside the control surface, $f(x,t) = 0$, are assumed to be negligible [27]. Therefore, formulation is composed of only surface integrals.

In application to cavity flow noise propagation, cavity is enclosed with a rectangular surface that is D (depth of the cavity) distance away from the cavity opening. Location of the integral control surface is selected such that it does not interact with the turbulence core region or the shear layer to provide an efficient control surface to FW-H method, as shown in Fig. 2.5.

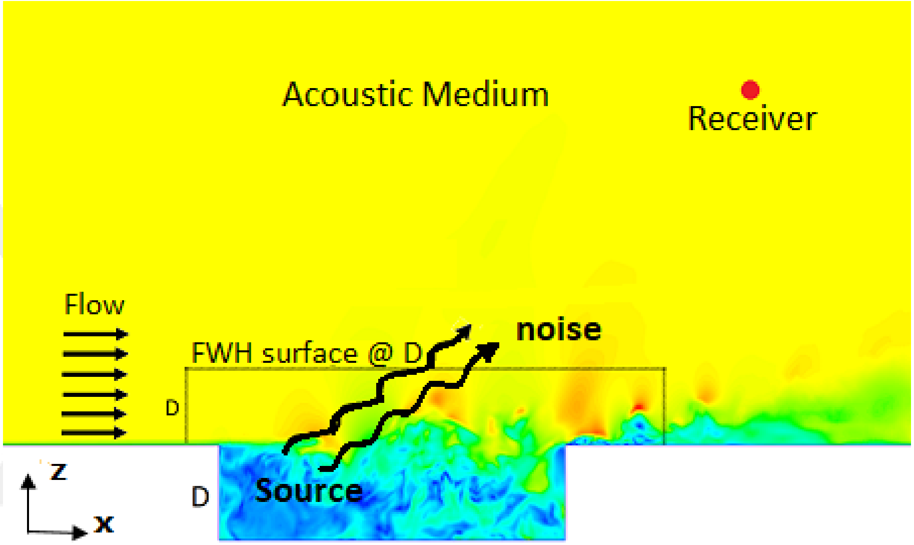

Figure 2.5: FW-H control surface for cavity flow application

2.3.2 Acoustic Data Processing

Noise environment of cavity flows is a result of complex flow around the cavity geometry. To obtain the acoustic environment, unsteady pressure data is post-processed to obtain acoustic characteristics, specifically sound pressure level (SPL) and pressure spectrum at the location of interest. This section is devoted to unsteady data processing to obtain the acoustic field in cavity flows.

Level of accuracy in acoustic post-processing is proportional to the length of unsteady data, which has drawback of increased computational cost. To minimize the effects of data length on acoustic post-processing, ensemble averaging is utilized. CFD simulations in the present study have 30,000 unsteady pressure data. First 5,000 data is ignored due to dominant transient effects. Rest of the data is employed in computational experiment with ensemble averaging. Acoustic data for each of the blocks is averaged to gather the overall acoustic response of the simulation. It is observed that blocks with 5,000 unsteady data length for spectral analysis and 1,000 data length for sound pressure levels and 50% overlap of blocks rendered the most compatible acoustic properties with experimental data.

2.3.2.1 Overall Sound Pressure Level (OASPL)

Overall sound pressure level (OASPL) is the relative pressure with respect to the ambient pressure of a medium through which sound waves propagate. It is an indication of fluctuations in flow. That is, the higher the OASPL at a location, the higher in magnitude the fluctuations are. Also, OASPL indicates the noise intensity in the domain of interest.

OASPL is given by:

$$\text{OASPL [dB]} = 20\log\left(\frac{P_{\text{rms}}}{P_{\text{ref}}}\right) \tag{2.3.2}$$

where P_{rms} is the root-mean-square pressure normalized by the minimum audible soundby human ear, which is $P_{\text{ref}} = 2 \times 10^{-5}$ Pa. P_{rms} is obtained by integration of unsteady pressure data as given by:

$$P_{\text{rms}} = \sqrt{\frac{\sum_{i=1}^{N}(P_{\text{instantaneous}} - P_{\text{mean}})^2}{N}} \tag{2.3.3}$$

where N is the number of data samples, $P_{\text{instantaneous}}$ is the instantaneous unsteady pressure data collected at each time step during simulation, and P_{mean} is the mean of overall unsteady pressure data at each of data points.

2.3.2.2 Spectral Analyses and Fast Fourier Transform (FFT)

Pressure spectrum or sound spectrum in acoustics represents the amount of pressure fluctuations with respect to each of individual frequencies, measured in vibrations per second (Hertz, Hz). A pressure spectrum is obtained through spectral analyses.

In spectral analyses, sequence of unsteady pressure data is converted from time domain to frequency domain and decomposed into oscillations with varying lengths and scales. When decomposed data is summed up in frequency domain, critical frequencies are obtained, which address the location of distributed average power as a function of frequency. Accordingly, it indicates the modal frequencies at which pressure fluctuations are enormous. For survivability of structures exposed to intense acoustic environment, modal frequencies and peak magnitudes are determined through spectral analysis.

Time domain data is converted into frequency domain through Fast Fourier Transform (FFT), which is a specialized form of Fourier transform that handles the discrete data.

2.3.2.3 Rossiter Modes

Cavity modes are vital to cavity resonance. Therefore, prediction of the modes within an acceptable accuracy by a sample formula is valuable. In this respect, Rossiter (1960) [28] proposed a semi-empirical formula for the calculation of acoustic modes of cavities at high speed flows. Rossiter [28] suggested that frequencies of periodic fluctuations within the cavity are directly proportional to free stream velocity and inversely proportional to cavity length. Heller (1970) [29] modified the classical Rossiter formula to account for the local speed of sound within the cavity, as provided in Eqn. 2.3.4.

$$f_m = \frac{U_\infty}{L}\left[\frac{m-\alpha}{M_\infty(1+(\frac{\gamma-1}{2})M_\infty^2)+\frac{1}{\kappa}}\right] \tag{2.3.4}$$

where f_m is the frequency of the m^{th} mode, L is the cavity length, M_∞ is the free stream Mach number, α and κ are empirical constants.

Although Rossiter's method provides reasonable prediction of frequencies of acoustic modes, there is no such simple and reliable method in the prediction of modal peak magnitudes.

CHAPTER 3

ASSESSMENT OF TURBULENT FLOW MODELS FOR CAVITY FLOWS

Navier-Stokes equations can only be solved numerically since there is no analytical solution. Computational Fluid Dynamics (CFD), in this respect, is a powerful tool that provides various numerical approaches to solution of N-S equations. Depending on the problem of interest, an appropriate numerical method needs to be determined first. In this respect, various numerical methods are examined in this chapter for the solution of cavity flows at transonic speeds.

3.1 CFD Validation Test Case: M219 Cavity

It is a common practice in CFD community that any CFD method is validated first for applicability to the issued problem. Validation can be made with respect to wind tunnel and/or existing CFD results.

In this section, M219 test cavity is examined to assess suitability of various solvers available in the commercial FLUENT code for cavity flow solutions. Investigated CFD methods cover k-ω SST and RNG k-ϵ URANS models, and S-A DES, S-A DDES, and k-ω SST based IDDES methods. Ross & Peto [5] conducted wind tunnel tests for the clean M219 configuration. M219 test case is an open type cavity with $L/D = 5$ and $W/D = 1$. It has $L = 0.508$ meters and $W = D = 0.1016$ meters dimensions, as shown in Fig. 3.1. Operating conditions for the test section are $M = 0.85$, $T = 251.77\ K$, Re $= 6.7 \times 10^6$, $P = 63.1\ kPa$ [5].

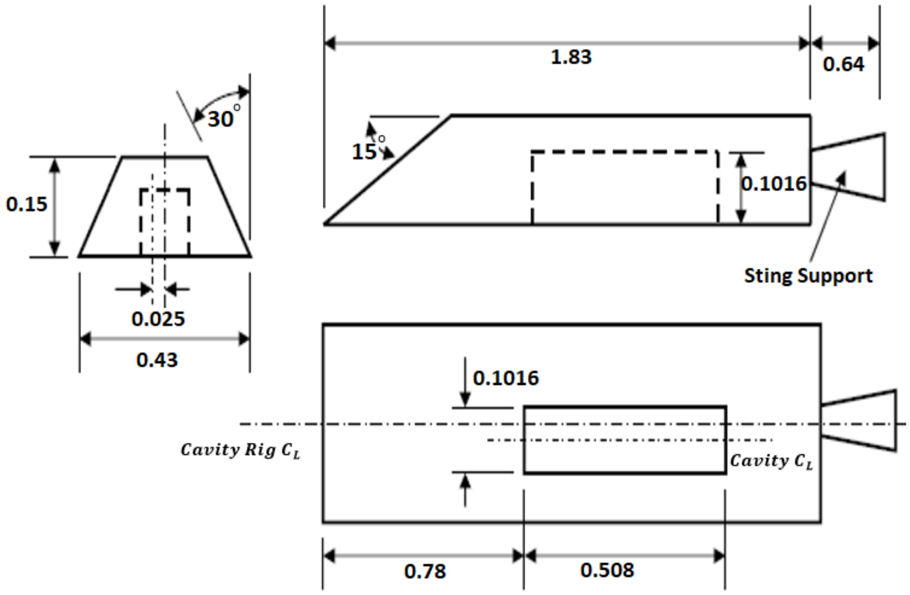
1.83
0.64
30°
15°
0.15
0.1016
0.025
0.43
Sting Support
0.1016
Cavity Rig C_L
Cavity C_L
0.78
0.508

Figure 3.1: Experimental rig of M219 cavity model (dimensions in meters, adapted from Nayyar (2005) [4])

In the experiment conducted by Ross [5], 10 pressure tabs were located at the cavity centerline on the cavity ceiling, starting from x/L = 0.05 and located at equi-distance, as illustrated in Fig. 3.2. At each of these pressure tabs, instantaneous pressure was measured and post-processed to obtain OASPL and root-mean-square pressure levels, which are the indicators of the acoustic field in the cavity.

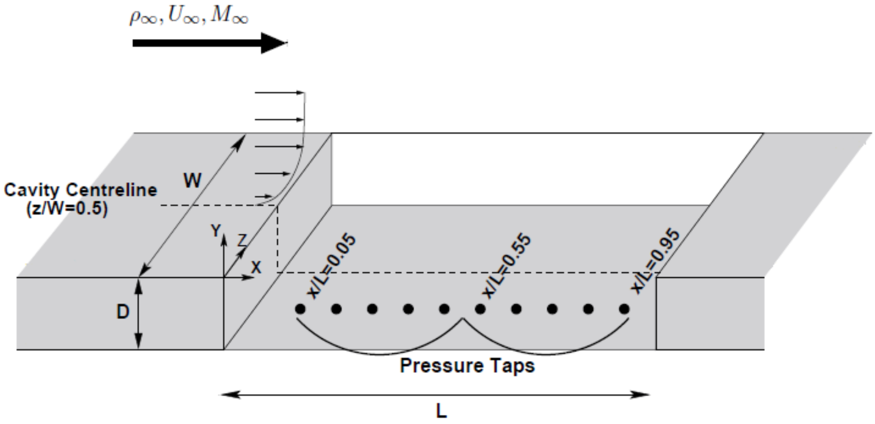
$\rho_\infty, U_\infty, M_\infty$
Cavity Centreline
(z/W=0.5)
W
Y
Z
X
D
x/L=0.05
x/L=0.55
x/L=0.95
Pressure Taps
L

Figure 3.2: Locations of pressure tabs at the M219 test cavity baseline [4]

3.2 URANS Models in Cavity Flow Solutions

Complexity of cavity flows requires higher order scale resolving turbulence treatment such as application of DNS, LES and etc. However, because of high computational burden of LES and DNS methods, researchers still desire to benefit from methods with lower costs with acceptable accuracy. URANS methods are examples to these alternative methods for cavity flow solutions. Although they are not impeccably suited for acoustic noise prediction due to their averaging and modeling nature, applicability of URANS models still deserve to be investigated for cavity flows. Hence, prediction capability of URANS with the k-ω SST and RNG k-ϵ turbulence models is discovered in this section. The study is discussed in the next subsections.

3.2.1 Computational Domain

The M219 test cavity is selected for the computational study of the URANS approach with the aforementioned turbulence models, as well as to evaluate three variants of detached eddy simulation (DES) approach, which are discussed separately. The cavity configuration has a length-to-depth ratio of $L/D = 5$, and width-to-depth ratio of $W/D = 1$. An unstructured mesh is generated as illustrated in Fig. 3.3. The computations are conducted at a Mach number of 0.85, and Reynolds number of 6.7×10^6, based on the cavity length (0.508 m).

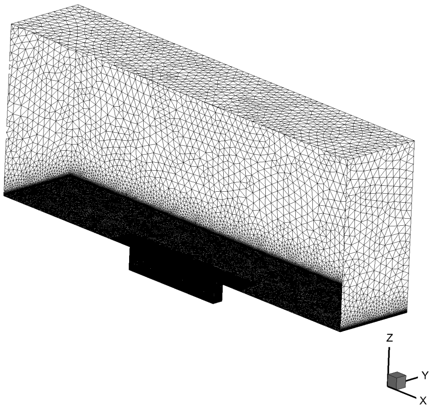

Figure 3.3: Sample computational domain for M219 geometry

3.2.2 Grid Independency

First step into a CFD solution is to conduct a grid independency study to determine the minimum grid requirement for an acceptable grid independent solution. In particular, independency of the overall sound pressure level (OASPL) is checked here on the centerline of the cavity ceiling. A total of 5 different grids are considered with the grid size and solution parameters that are provided in Table 3.1. $y+$, in the table, shows the dimensionless physical thickness of the first grid layer in the boundary layer (B/L). This parameter is quite important because it directly affects the B/L resolution. General cell size distribution within the cavity is crucial in resolution of complex flow characteristics. On the other hand, grid size has a direct influence on the computational cost, and therefore the best compromise conditions should be established.

Table 3.1: Parameters for URANS Grid Convergence Study

	Grid 1	Grid 2	Grid 3	Grid 4	Grid 5
$y+$	1	0.5	0.667	0.3	0.667
First Layer Thickness [$\times 10^{-6}$ m]	2	0.9	1	0.6	1
Number of Layers in B/L	30	51	41	61	41
Cell Size within the Cavity [mm]	3.5	3	2	2	1.75
Grid Volume Size ($\times 10^6$)	8	20	19	26	24

Solution on each grid is obtained through the k-ω SST and RNG k-ϵ turbulence models as indicated earlier. The attained OASPL results are compared to the experimental results of Ross [5] as shown in Fig. 3.4. It is evident from the comparisons that the URANS models captured the general trend of OASPL along the centerline of cavity ceiling, as the grids were refined, in particular within the cavity volume (Grid 3 and 4). The k-ω SST turbulence model is more grid-dependent for OASPL predictions, as shown in Fig. 3.4a, than the RNG k-ϵ turbulence model, which provides similar level of accuracy for each of the grids used as shown in Fig. 3.4b.

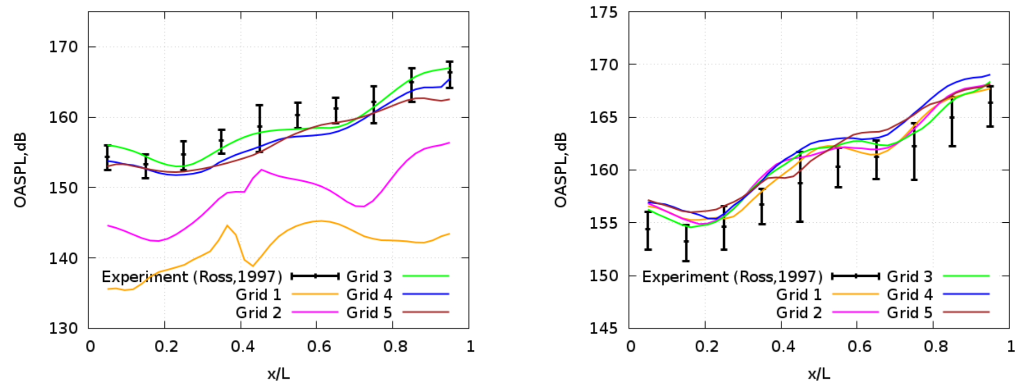

(a) k-ω SST model

(b) RNG k-ϵ model

Figure 3.4: Results of URANS turbulence models for grid convergence study ($M = 0.85$, 2^{nd} order scheme, $\Delta t = 2 \times 10^{-5}$ s)

It is interesting though to observe that the k-ω SST model yields results that have strong dependence on the computational grid, unlike the RNG k-ϵ model, which provides almost identical levels of accuracy for all of the grids used. The RNG k-ϵ model yielded results on Grid 1 (coarse) not far from those on the other grids, while the k-ω SST model performed quite poorly on the same mesh. The mesh resolution, particularly in the vicinity of the walls and inside the cavity, seems to have their own distinct effects on noise predictions of cavity flows. Grid 3 predictions with the k-ω SST turbulence model seem to be the best among the other grids when compared to the experimental data.

Another important aspect of the cavity flow solutions is their frequency content. The results for Grid 3 post-processed with Fast Fourier Transform (FFT) are shown in Fig. 3.5, for the root-mean-square pressure at the $x/L = 0.95$ point on the cavity ceiling. Computational results for the frequency spectrum of the cavity are compared to experimental data by Ross [5] as well as analytically modeled Rositter frequencies. URANS models, particularly those with the k-ω SST model, could predict the cavity dominant modal frequencies with reasonable accuracy. However, both turbulence models overpredicted the 2^{nd} and 3^{rd} modal amplitudes. Overprediction by the RNG k-ϵ model was less than that by the k-ω SST model. The 4th modal amplitude was not captured by the k-ω SST model, while RNG k-ϵ model had good prediction of it.

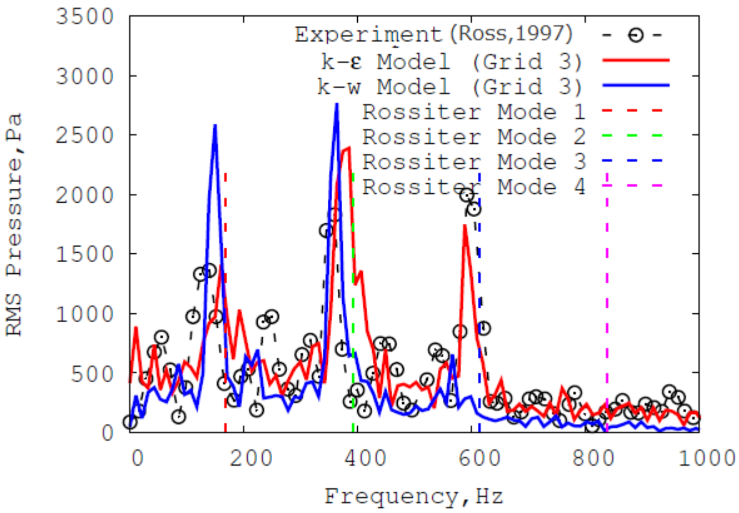

Figure 3.5: FFT obtained RMS pressure at $x/L = 0.95$ in comparison to Rossiter modes and experimental data ($M = 0.85$, 2^{nd} order scheme, $\Delta t = 2 \times 10^{-5}$ s)

3.2.3 Effects of Order of Spatial Discretization Scheme

Cavity flows exhibit characteristics that stem from strong coupling between the cavity flow and acoustics. The mutual interactions cause sustained oscillations in the flow variables. Therefore, cavity flow simulations rely strongly on appropriate turbulence models and accurate numerical methods. In this respect, 2^{nd} order and 3^{rd} order numerical schemes are utilized in the solution of cavity flows. Results are provided in terms of OASPL and RMS pressure in Fig. 3.6 for k-ω SST model and in Fig. 3.7 for RNG k-ϵ model.

When the effects of order of spatial discretization on k-ω SST and RNG k-ϵ results are compared, it is observed that the k-ω SST model results seem more sensitive to the order of numerical scheme and unexpectedly turns out to be better with the 2^{nd} order discretization approach when compared with the experimental data [5]. It is because the grid convergence is conducted with 2^{nd} order numerical scheme and the same grid is utilized for the 3^{rd} order scheme. The results show that the optimum grid for a numerical scheme may not be the best grid for another scheme. Therefore, 3^{rd} scheme requires further improvements on the grid.

The 3^{rd} order scheme with the k-ω SST model overestimates OASPL along the centerline of cavity ceiling while the 2^{nd} order scheme with the k-ω SST predicts the OASPL within the experimental envelope, as illustrated in Fig. 3.6a.

Effects of order of spatial discretization on RMS pressure levels for the k-ω SST model are shown in Fig. 3.6b. While the 3^{rd} order scheme is able to predict the modal frequencies, the 2^{nd} order scheme could not capture one of the dominant modes, specifically the mode at $\sim$ 600 Hz.

Although the 3^{rd} order scheme seems to predict the pressure spectra better than 2^{nd} order scheme, both spatial discretization schemes are unable to predict the modal amplitudes accurately. None of the numerical schemes could predict the modal amplitudes because of the averaging nature of URANS models, as shown in Fig. 3.6b.

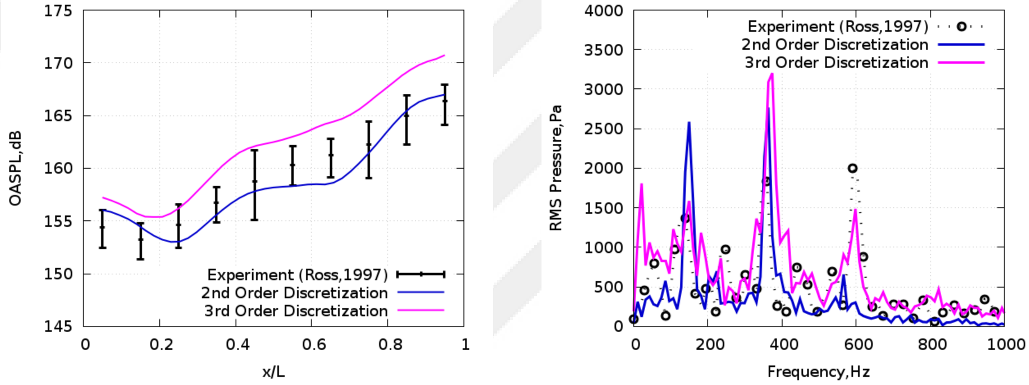

(a) OASPL

(b) RMS Pressure

Figure 3.6: Order of discretization effects on cavity noise prediction via k-ω SST model with experimental data [5] ($M = 0.85$, $\Delta t = 2 \times 10^{-5}$ s)

The RNG k-ϵ model, on the other hand, yields quite similar results with both the 2^{nd} and 3^{rd} order spatial schemes along the centerline of cavity ceiling as shown in Fig. 3.7a. Effects of spatial discretization on pressure spectra for RNG k-ϵ model are compared in Fig. 3.7b. Both the 2^{nd} and 3^{rd} order schemes are able to predict the frequencies of two dominant modes. Although the 3^{rd} order scheme approximates the second mode better in magnitude, it misses the first mode and underpredicts the magnitude of the third mode. Therefore, none of the 2^{nd} and 3^{rd} order spatial schemes has superiority to each other in prediction of pressure spectra for the RNG k-ϵ model.

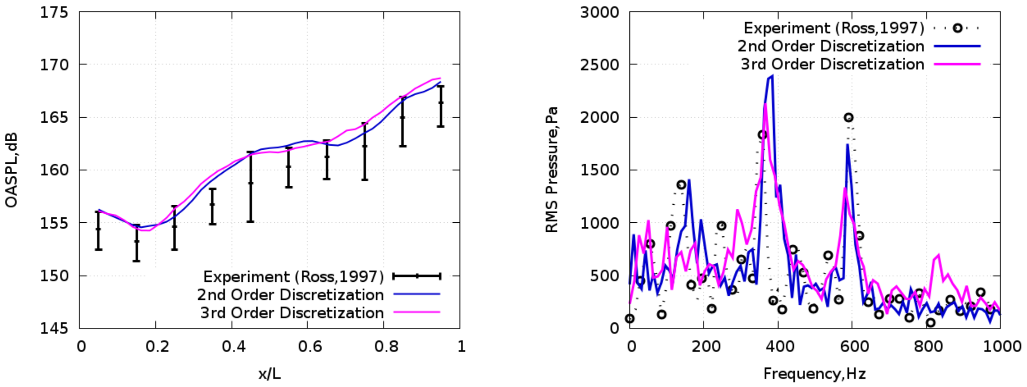

(a) OASPL

(b) RMS Pressure

Figure 3.7: Order of discretization effects on cavity noise prediction via RNG k-ϵ model with experimental data [5] ($M = 0.85$, $\Delta t = 2 \times 10^{-5}$ s)

3.3 Detached Eddy Simulations in Cavity Flow Solutions

Detached Eddy Simulation (DES) approach utilizes the best aspects of URANS and Large Eddy Simulation (LES) approaches. DES is a widely accepted alternative solution method to cavity flows. The DES methods make use of URANS approach within the B/L, and LES elsewhere. Therefore, the DES methods are expected to provide improved results for cavity flow solutions. However, the aforementioned issues existing in DES may have some hindering effects on the accuracy compared to URANS methods. DES with the Spalart-Allmaras (S-A) turbulence model, Detached DES (DDES) with S-A, and k-ω SST based Improved Delayed DES (IDDES) methods are investigated in this section to assess their suitability to cavity flows.

3.3.1 Effects of Detached Eddy Simulation Variants

Grid 3 of URANS grid convergence study is utilized in simulations of DES models because the grid is fine enough to meet the needs of DES models. $\Delta t = 1 \times 10^{-5}$ time step is used. Results for OASPL and RMS pressure are shown in Fig. 3.8. It is clear from Fig. 3.8a that the DDES and IDDES methods yield OASPL with similar accuracy. DES, on the other hand, seems to perform poorly for the current problem.

When Fig. 3.8b is analyzed more closely, it is observed that IDDES captures the peak fluctuation level, which occurs near the aft wall at $x/L = 0.95$, more accurately than the other approaches. IDDES also seems to have produced improved results for the OASPL along the centerline of cavity ceiling in comparison to experimental data. Figure 3.8b shows that IDDES accurately predicts both the modal frequencies and amplitudes of dominant modes in the pressure spectrum. DDES can predict the modal frequencies with a level of accuracy although it has a significant deviation from the modal amplitudes compared to IDDES. DES, on the other hand, performs the poorest results in terms of both OASPL and pressure spectrum in Fig. 3.8 for the current problem. As a conclusion, IDDES is considered as the most suitable model for the highly unsteady and turbulent cavity flow problems among the other DES variants considered here.

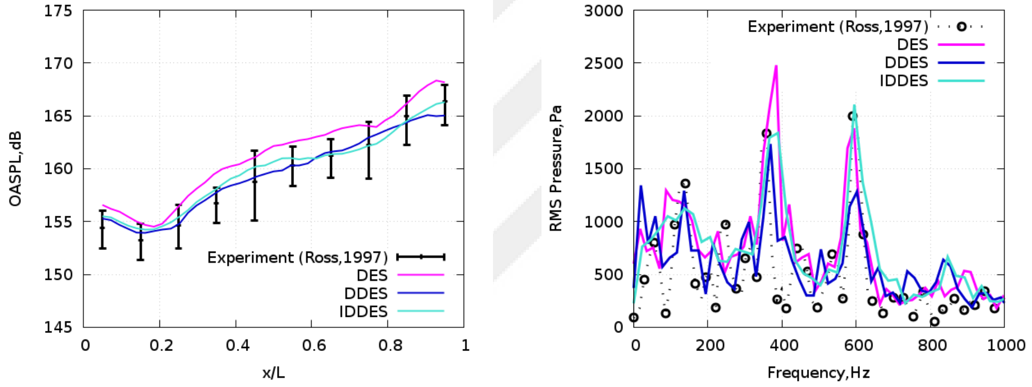

(a) OASPL

(b) RMS Pressure at $x/L = 0.95$

Figure 3.8: Alternative DES methods predictions to cavity noise levels with experimental data [5] ($M = 0.85$, 3^{rd} order scheme, $\Delta t = 1 \times 10^{-5}$ sec.)

3.3.2 Grid Independency

A grid convergence study is also conducted for IDDES method to determine the grid resolution that provides the highest computational efficiency without loss of accuracy. Since IDDES method utilizes URANS modeling approach within the boundary layer regions and LES outside, the best performing grid properties in URANS grid convergence study is utilized as the baseline grid (Grid 1-I). Only the grid size within the cavity (i.e. LES region) is refined such that the grid size is halved. Grid properties are shown in Table 3.2.

Table 3.2: Parameters for IDDES Grid Convergence Study

	Grid 1-I	Grid 2-I
Cell Size within the Cavity [mm]	2	1
Grid Volume Size ($\times 10^6$)	19	27

Results of the grid convergence study are compared in terms of both OASPL and frequency spectrum, as illustrated in Fig. 3.9. It is observed that further refinement of the cell size within the cavity does not have any significant effect on the accuracy of the simulations. Therefore, Grid 1-I is utilized in following simulations because of its computational efficiency without loss of accuracy.

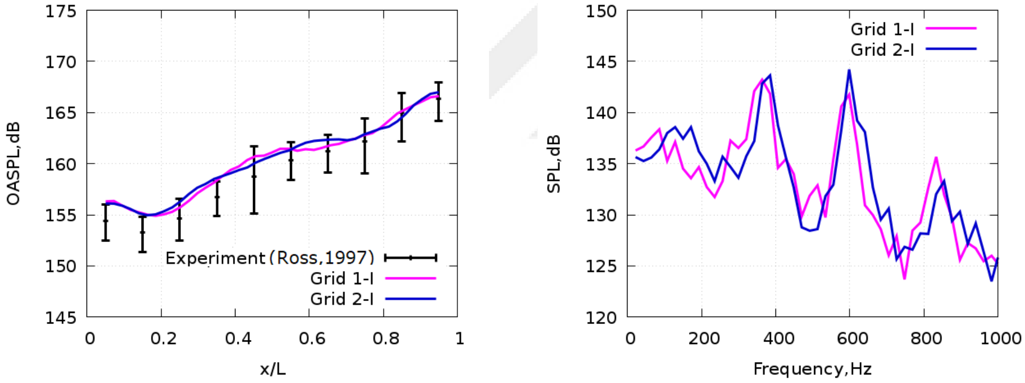

(a) OASPL

(b) Pressure spectra at $x/L = 0.95$

Figure 3.9: Results of IDDES method grid convergence study ($M = 0.85$, 3^{rd} order scheme, $\Delta t = 1 \times 10^{-5}$ s)

3.3.3 Effects of Time-step

One of the crucial parameters in the solution of cavity flows is the time step. Time step is important for both stability of the numerical solution and the prediction of acoustic environment around the problem of interest. Time step directly affects the stability of a numerical solution through Courant-Friedrichs-Levy (CFL) condition, which relates time step of the smallest cell size in the computational domain and flow velocity. In other words, maximum allowable time step is bounded by CFL condition. It is also important in terms of the computational cost of the numerical solution. As the time step decreases, number of iterations required to obtain data for the same time interval increases, resulting in higher computational costs.

Another limitation on time step size comes from the required frequency resolution. Time step directly determines the frequency resolution through the Nyquist frequency. As the time step decreases, more and more frequencies are resolved that provide improved prediction of pressure spectrum in cavity flow solutions. Therefore, there is a compromise between computational time and the frequency resolution of the solution. In this respect, two different time step sizes, $\Delta t = 2 \times 10^{-5}$ s and $\Delta t = 1 \times 10^{-5}$ s, are investigated in the solution of cavity flow with IDDES method. Results are provided in Fig. 3.10.

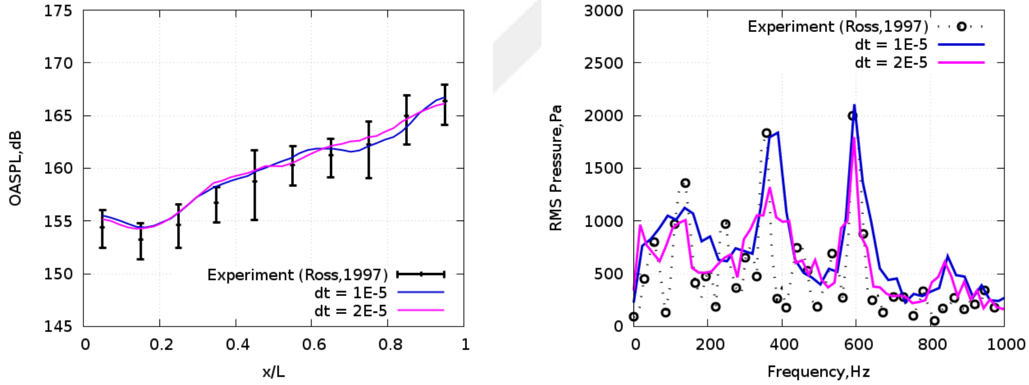

(a) OASPL

(b) RMS Pressure at $x/L = 0.95$

Figure 3.10: Effects of time step on the cavity flow solutions ($M = 0.85$, 3^{rd} order scheme)

It is observed from Fig. 3.10a that both time step sizes used here provide quite similar predictions of OASPL. The major effect of time step is revealed in the prediction of pressure spectrum. As it is clearly seen in Fig. 3.10b, reduced time step considerably improves prediction of the modal frequencies and amplitudes, more accurately. $\Delta t =$

1×10^{-5} s time step seems to yield reasonable accuracy not only for the frequencies of dominant modes but also for their amplitudes.

Another important parameter in solution of scale resolving turbulence models is the shear layer velocity profile. Instantaneous streamwise velocity data is collected at each time step throughout the simulation at constant x-lines along the centerline of cavity ceiling. Instantaneous velocity data is then averaged to compute the shear layer velocity profiles along the cavity, and it is compared to experimental data [30] as shown in Fig. 3.11.

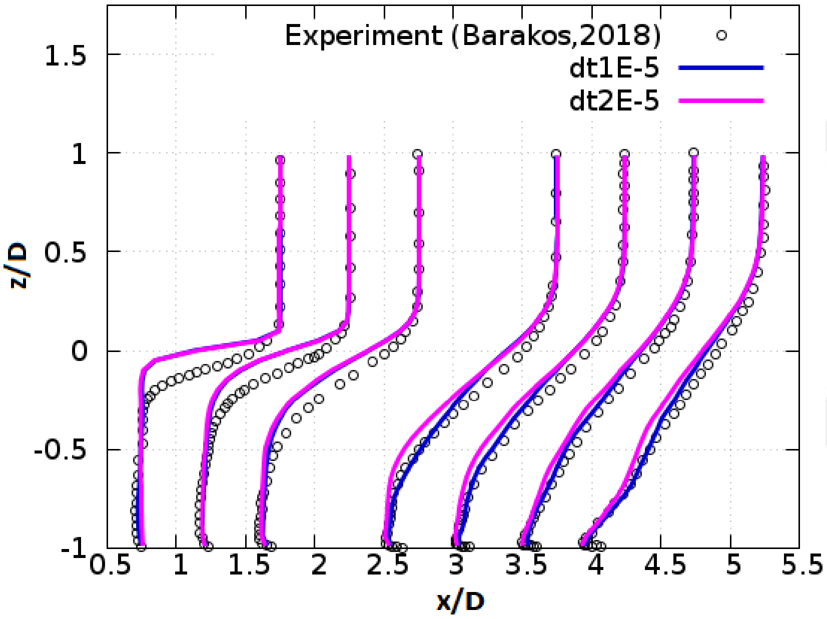

Figure 3.11: Time-step dependency of IDDES shear layer streamwise mean velocity profiles. The horizontal axis is scaled to $U/U_\infty + x/D$ ($M = 0.85$, 3^{rd} order scheme)

It is evident from Fig. 3.11 that $\Delta t = 1 \times 10^{-5}$ s time step provides improvement in prediction of shear layer streamwise velocity distributions compared to $\Delta t = 2\times10^{-5}$ s, with increased accuracy towards aft of the cavity. However, in the front regions of cavity opening, where massive flow separation takes place, shear layer streamwise velocity profile predictions are not satisfactory for both time steps used. This could be attributed to the massive flow separation around the leading edge of the cavity that cause high gradients in the flow variables. In this region, IDDES model has difficulty because of the switching from URANS to LES mode.

3.3.4 Turbulence Models Comparison for Cavity Flow Solutions

In the present work, k-ω SST and RNG k-ϵ URANS models and DES, DDES, and IDDES methods are compared for related parameters to obtain the applicability of turbulence models of interest. The best performing models are determined by comparing the solutions in terms of OASPL and RMS pressure along the centerline of the cavity ceiling as illustrated in Fig. 3.12.

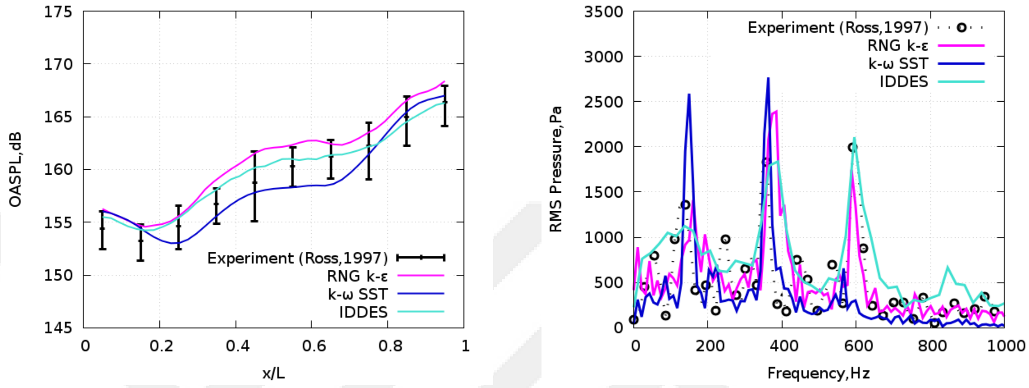

(a) OASPL (b) RMS Pressure at $x/L = 0.95$

Figure 3.12: Turbulence models comparison on cavity flow solutions $M = 0.85$, 3^{rd} order scheme, $\Delta t = 1 \times 10^{-5} s$)

When Fig. 3.12 is inspected more closely, it can be observed that IDDES appears to produce the best comparison with the experimental data among all the turbulence models employed. Although k-ω SST and RNG k-ϵ URANS models can predict the trend of OASPL along the centerline of cavity ceiling, they are not as effective as the IDDES solutions as shown in 3.12a. When pressure spectrum is considered, superiority of IDDES method over URANS models is clearer in Fig. 3.12b. Therefore, IDDES method is considered to be the most suitable one among all the turbulence models employed in the present study.

YÖK

CHAPTER 4

RESULTS AND DISCUSSION

In this chapter, various cavity configurations in transonic flow regime are explored. Cavity configurations include a clean cavity, cavity with a generic store and cavity with doors at various angles to the cavity side walls. Farfield noise characteristics of clean cavity flow are also examined. IDDES turbulence model with 3^{rd} order numerical scheme and $\Delta t = 1 \times 10^{-5}$ s time step is utilized for the rest of the analyses as a result of previous chapter.

4.1 Cavity Configurations

In exploration of cavity configurations, clean cavity (cavity with no missile, no doors etc.) is considered first. After then, effects of a generic tangent-ogive store and cavity doors at various angles on the flow field and noise environment of cavities are analyzed and the results are compared to those of the clean cavity in terms of OASPL and frequency spectra. Reynolds number effects on cavity flow and acoustic characteristics are also investigated.

4.1.1 Clean Cavity Flow

The main objective of the present work is to predict the flow and acoustic environment of cavities via CFD with an acceptable accuracy. Previous chapter has dealt with several numerical issues. Particularly grid resolution, time step, and Reynolds number effects have been studied providing hints to the meshing and numerical strategies to be used in this chapter. M219 test cavity is utilized as the clean cavity configuration.

Flow features at various times are looked into closely. Fig. 4.1 shows instantaneous Mach contours at various fractions of the oscillation period T of the most dominant noise generating structures. For one period, T, of the dominant cavity mode (f $\sim$ 600 Hz), cavity flow nearly completes a loop. Flow field at the starting time, t, and at the end of one period, $t + 5T/6$, are quite similar to each other.

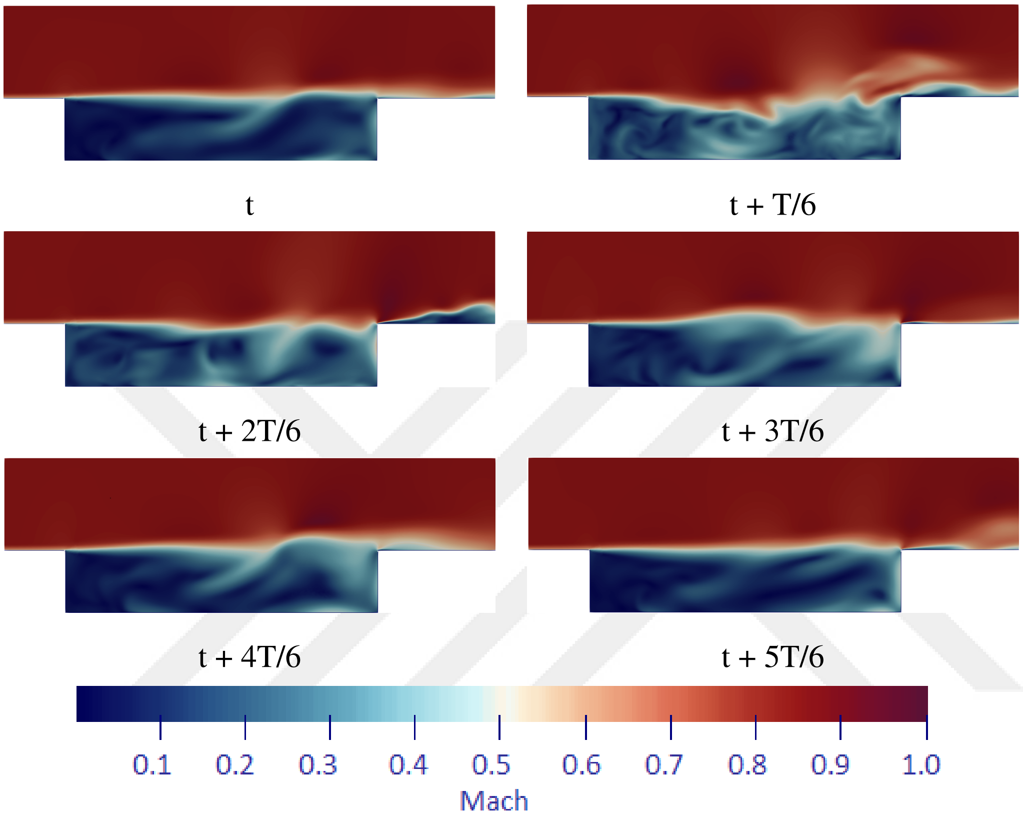
t

t + T/6

t + 2T/6

t + 3T/6

t + 4T/6

t + 5T/6

Figure 4.1: Instantaneous Mach contours at $1/6^{th}$ of period, T (0.00167 s), of the dominant mode (at $\sim$ 600 Hz).

It appears from the Mach contours that, despite the oncoming free stream Mach number is 0.85, local flow speeds go over Mach 1 along the shear layer, typical of transonic cavity flow situations. This, in turn, results in generation of shock waves that interact with the boundary layer and shear layer and contributes to the complexity of the flow. Unsteadiness and complexity of the cavity flow can be observed in Fig. 4.1. It can also be observed from the figure that cavity flow field is dominated by vortical flow structures that are extremely unsteady.

Further instantaneous flow visualizations are shown in Fig. 4.2 for the clean cavity configuration at the aforementioned spanwise offset planes. In flow visualizations, line integral convolution (LIC) technique is utilized. LIC is a technique that convolves a vector field to obtain streaking patterns which follow vector field tangents.

Flow visualizations in Fig. 4.2 on the offset planes demonstrate the 3-dimensionality of the flow field. There is a core vortex structure spanning over the cavity length accompanied by secondary vortical flows at the corner regions in all of the offset planes. It is observed from Fig. 4.2 that the extent and locations of the vortex structures in offset planes are not the same due to 3-dimensionality of the flow field.

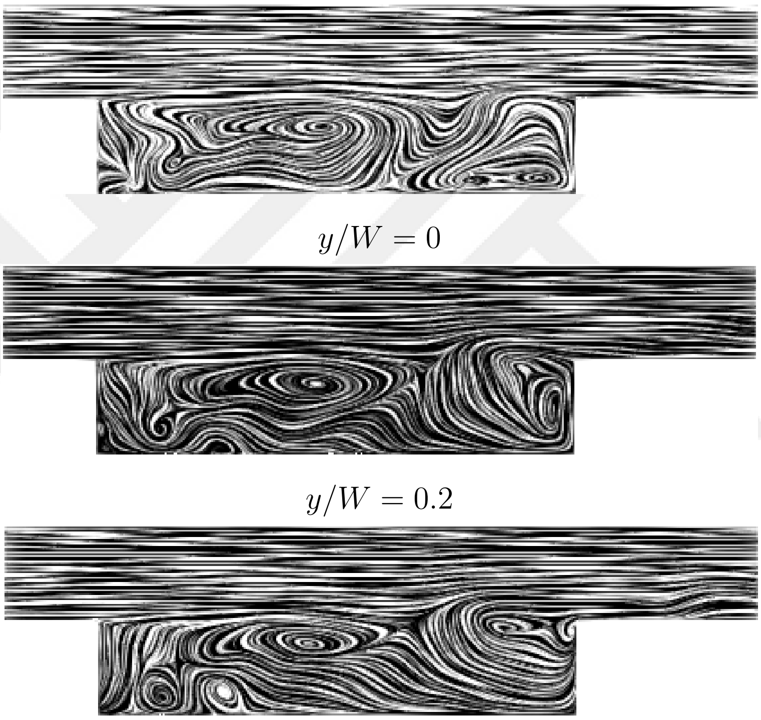

$y/W = 0$

$y/W = 0.2$

$y/W = 0.4$

Figure 4.2: Instantaneous spanwise line integral convolution (LIC) images at offset planes

The cavity front and aft walls flow visualizations are also shown in Fig. 4.3 that demonstrates the existence of spanwise flow components clearly. Shear layer reattachment and flow interactions around the cavity aft wall cause relatively more intense vortex structures around the trailing edge of the cavity.

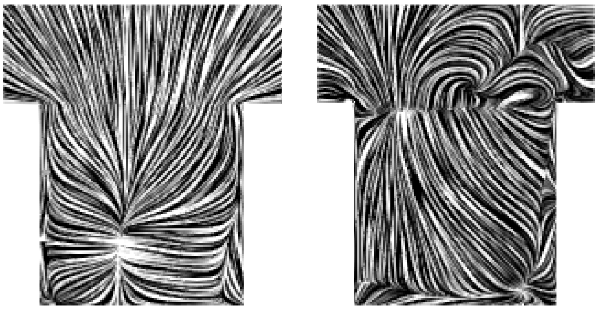

front wall

aft wall

Figure 4.3: Instantaneous streamwise line integral convolution (LIC) images

In this respect, Fig. 4.4 demonstrates OASPL distributions at spanwise offset locations corresponding to $y/W = 0$ (centerline), $y/W = 0.2$ and $y/W = 0.4$ over the cavity front wall, ceiling and aft wall.

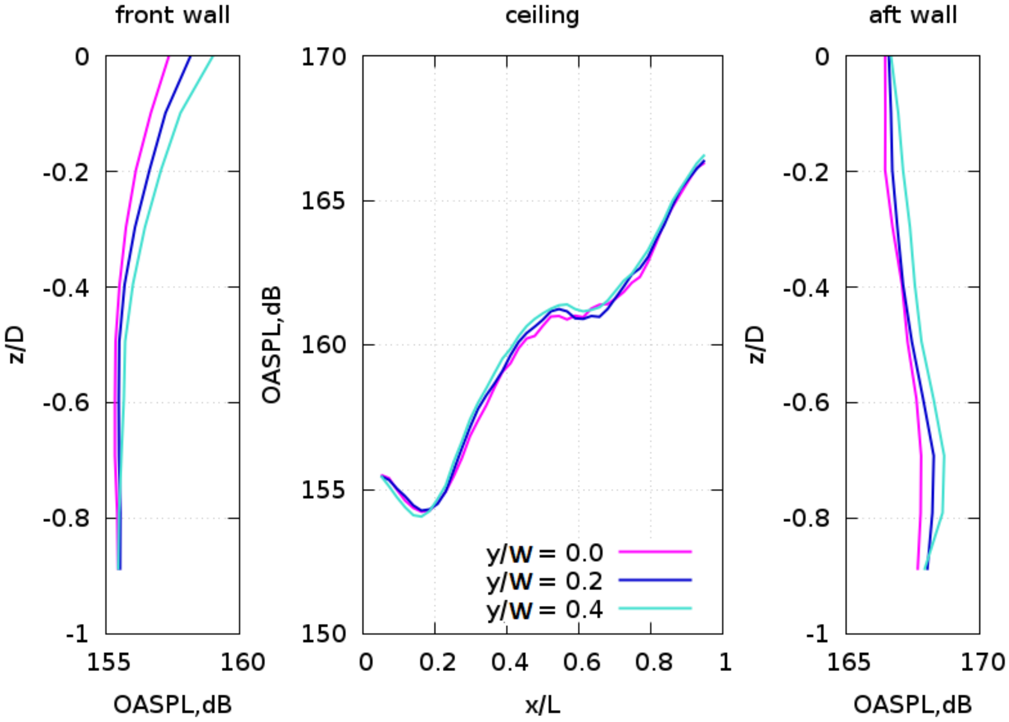

Figure 4.4: OASPL along $y/W = 0$, $y/W = 0.2$, and $y/W = 0.4$ over the front wall, ceiling and aft wall of the cavity

The results indicate that OASPL gets higher towards the cavity opening, i.e. $z = 0$, in the front wall of the cavity. As the offset distance increases from the cavity centerline (i.e. $y = 0$), noise intensity appears to increase around the cavity opening. Offset effects tend to disappear towards the cavity ceiling and OASPL is almost constant from $z/D = -0.6$ to the ceiling, as illustrated in Fig. 4.4 (left).

On the other hand, noise intensity almost stays constant at various offset locations considered as shown in Fig. 4.4 (center). As it is expected, noise intensity increases significantly towards the aft wall of the cavity. This is caused mainly by the shear layer attachment on the cavity aft wall. Accompanying feedback mechanism also develops within the cavity that triggers intense noise around this region.

Noise intensity at the aft wall of the cavity also has negligible sensitivity to spanwise offset locations as illustrated in Fig. 4.4 (right). Vertical variation of noise intensity along the cavity aft wall is also not substantial.

OASPL distribution over the symmetry plane of the cavity is also computed and the results are provided in Fig. 4.5. It can be observed from the figure that noise intensity around the cavity aft wall is higher as expected due to highly unsteady shear layer attachment on the aft wall. Therefore, aft wall region of an internal weapon bay requires careful placement of internal instrumentation during the design because of high noise intensity.

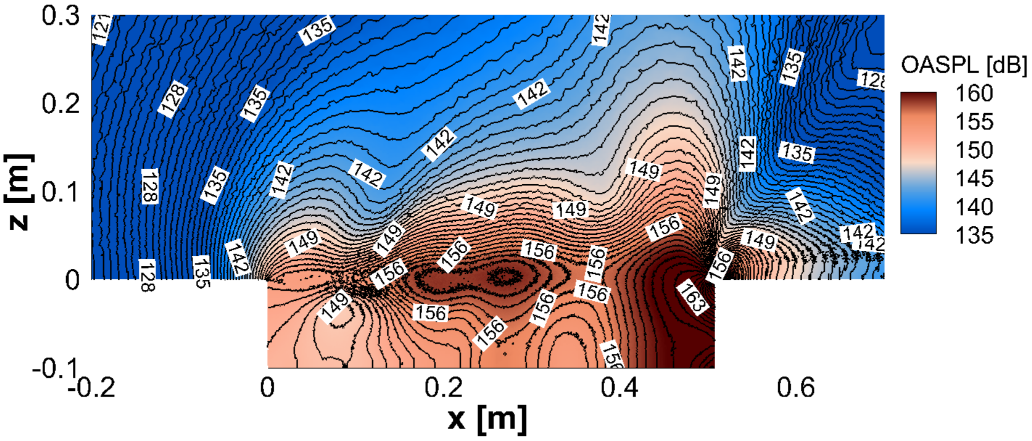

Figure 4.5: OASPL over the symmetry plane ($y/W = 0$) of the clean cavity

4.1.2 Cavity With A Generic Store

Knowles (2017) [6] conducted tests on an open cavity with a generic tangent-ogive, aft-mounted store at $M = 0.8$. The aim was to understand the effects of a store on the cavity flow physics and the acoustic environment. Length-to-depth ratio of the test cavity is $L/D = 5$ while width-to-depth ratio is $W/D = 1$, with $L = 160$ mm, $W = 32$ mm and depth $D = 32$ mm, which is approximately $1/3$ scale of M219 cavity. There were 27 pressure tabs on the cavity ceiling in three rows, one on the cavity center line while the other two have offsets [6]. The test section along with relative positions and geometries of generic tangent-ogive store and the cavity are provided in Fig. 4.6.

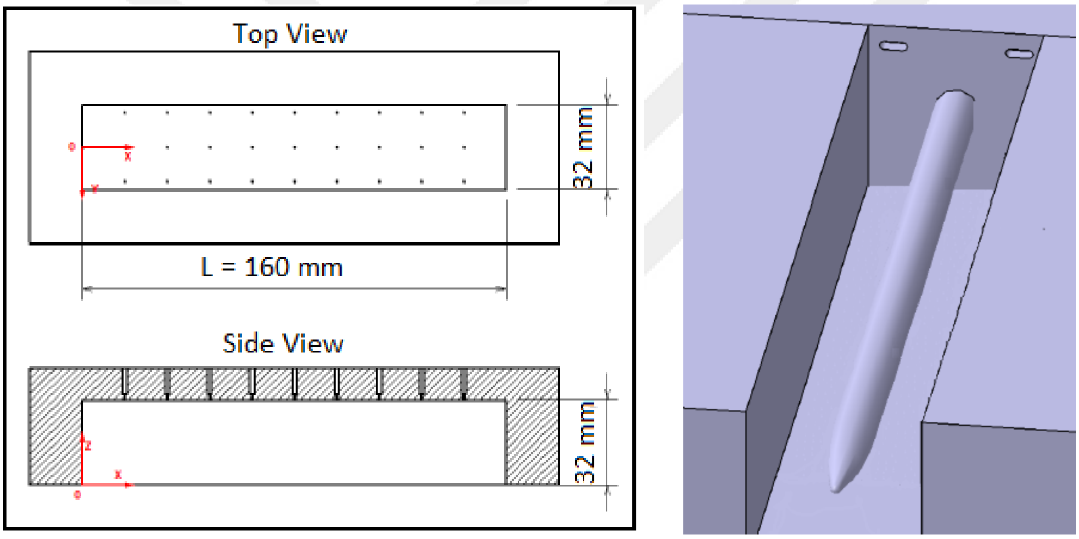

Figure 4.6: Cavity with Generic Store Test Section [6]

LIC flow visualizations for generic store-included cavity are shown in Fig. 4.7 at the spanwise offset planes that are used in the clean cavity case. Presence of the store in the cavity significantly affects the flow field within the cavity that it results in generation of more vortex structures around the store, as illustrated in Fig. 4.7 at $y/W = 0$. As it gets away from the centerline of the cavity at which store is located, effects of the store weaken and the flow field is similar to that in clean cavity case.

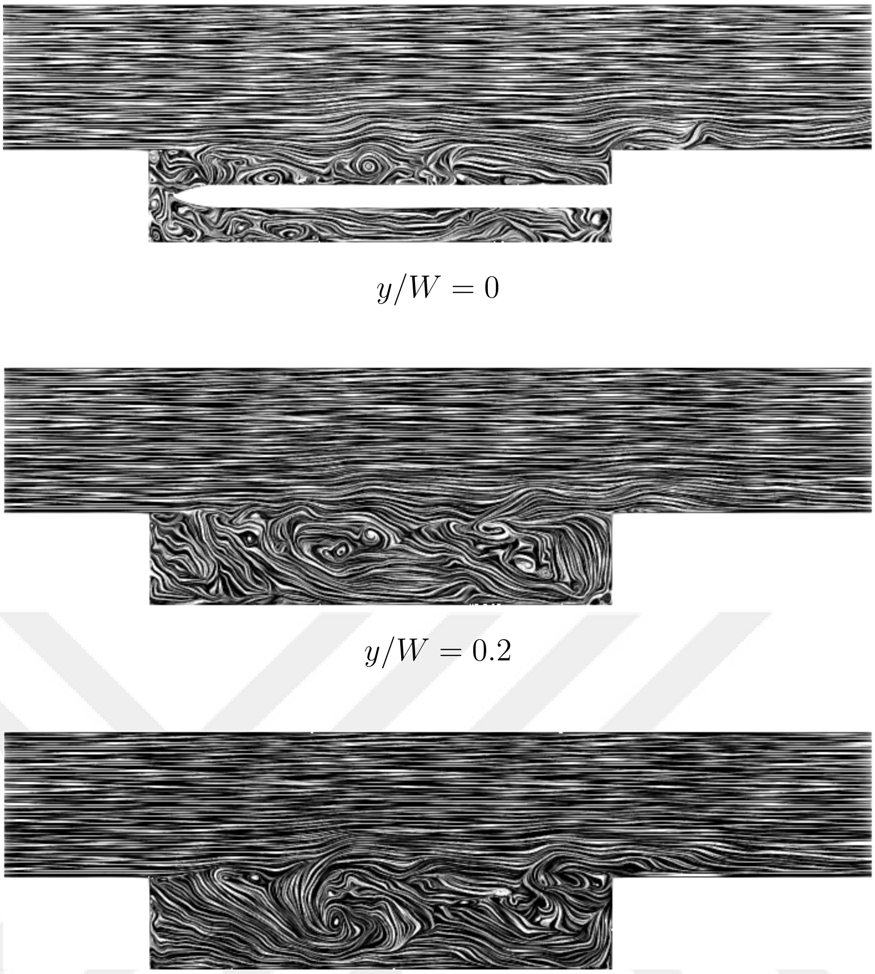

$y/W = 0$

$y/W = 0.2$

$y/W = 0.4$

Figure 4.7: Instantaneous spanwise LIC images for cavity with a generic tangent-ogive store

Flow visualizations on the store-included cavity front and aft walls are shown in Fig. 4.8. Spanwise flow is observed in the front and aft walls. In the aft wall, where the store is mounted, presence of the store triggers flow turn around the store and interactions with the corner vortices.

Front wall of the cavity is also affected by the presence of the store when compared to the clean cavity flow visualization. Presence of the store disturbs the separated flow at the cavity leading edge and contributes to the non-linearity of the flow in the front region of the cavity. Spanwise flow also exists around the leading edge of the cavity.

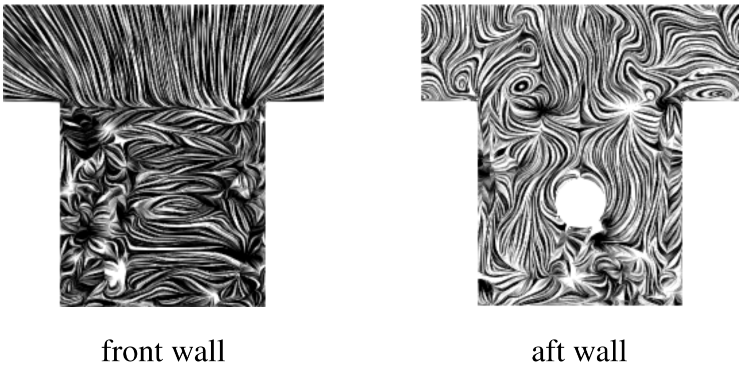
front wall
aft wall

Figure 4.8: Instantaneous streamwise LIC images for cavity with a generic store

Results of cavity with a generic store are presented in Fig. 4.9. OASPL prediction along the centerline of store included cavity is compared to both experimental data by Knowles (2017) [6] and clean cavity. As in the clean cavity case, IDDES also provides quite accurate OASPL predictions for cavity-with-store case, which consolidates the power of the computational model in cavity flow solutions.

Results for cavity-with-store are compared to the clean cavity solutions. It is observed that presence of a missile inside the cavity does not alter the noise intensity of the cavity significantly, as shown in Fig. 4.9. Presence of the current store does not break up the acoustic feedback mechanism generated within the cavity. Noise intensity towards the aft wall of the cavity increases as in the clean cavity configuration.

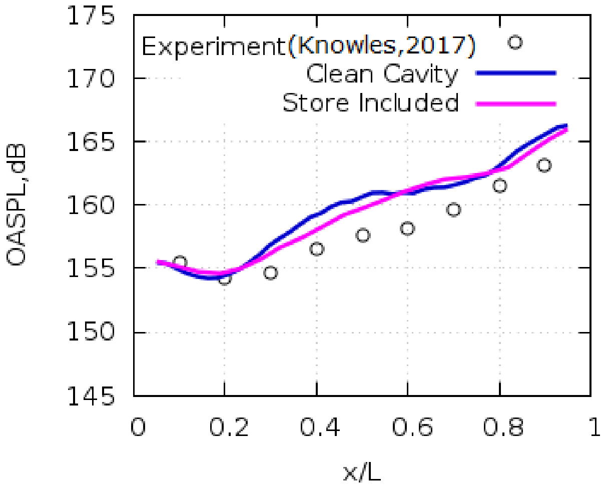

Figure 4.9: OASPL prediction of cavity-with-store configuration via IDDES model

4.1.3 Door Effects On Cavity Flow

During operation of the internal weapons bay, the cavity doors are first opened and then flow starts developing over it. Compared to the no-doors case, presence of the doors may have significant effects on the shear layer development and thereby acoustic feedback mechanism within the cavity. Therefore, understanding the flow physics in the presence of cavity doors is also substantial to cavity design.

This section is devoted to predict and understand the effects of the cavity doors on the flow field and acoustics. No transitional effects of the doors are considered. Rather, they are assumed to have already been positioned at some fixed angles, as illustrated in Fig. 4.10. For each doors orientation case though, re-meshing of the flow domain needs to be done.

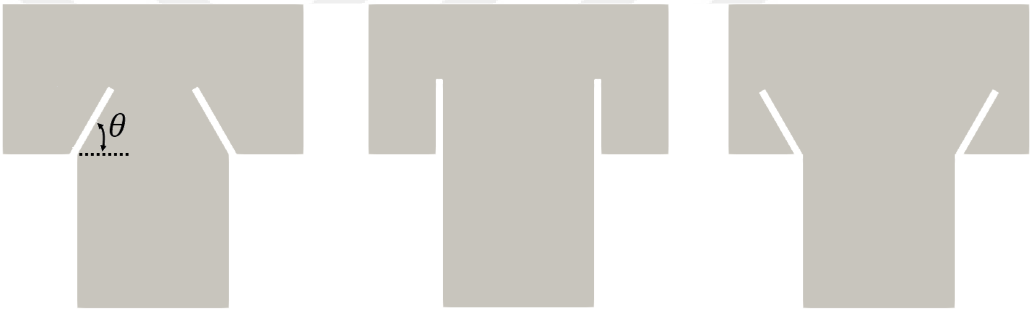

Figure 4.10: Doors at 60°, 90°, and 120°, respectively

4.1.3.1 Doors at 90° Orientation

Flow visualizations for the case with 90° door positions are provided in Fig. 4.11. The presence of the doors appears to cause major changes in the flow physics. The vertical alignment of the doors to the cavity opening confines spanwise variations in the shear layer and acoustic propagation. Hence, stronger interactions between them and the doors occur, which intensify the acoustic feedback mechanism. Also, separated flow is observed around the cavity doors which triggers more intense turbulence around the doors and the cavity. Interactions of the turbulent wakes with each other and the shear layer are clear in Fig. 4.11 at $z/D = 0.05$, which is near the doors and close to the shear layer.

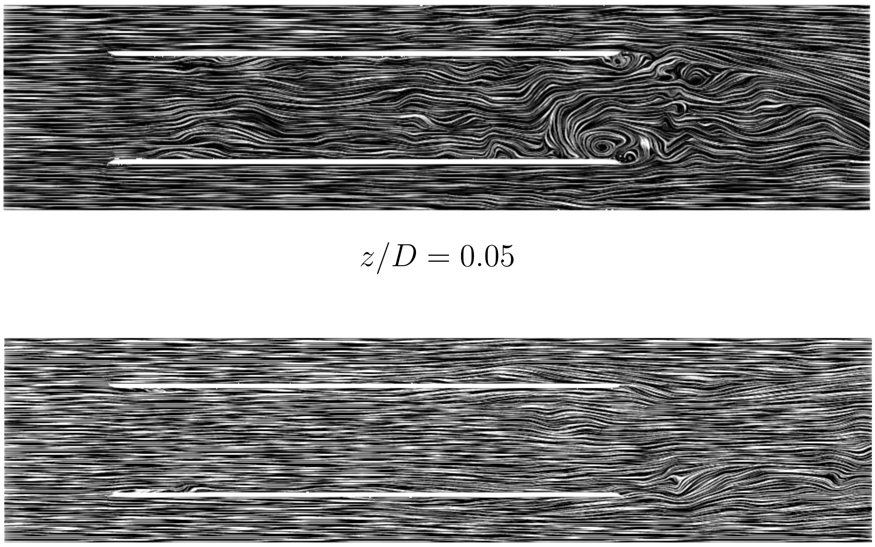

$z/D = 0.05$

$z/D = 0.45$

Figure 4.11: Instantaneous LIC images at $z/D = 0.05$ and $z/D = 0.45$ for cavity doors at 90°

Streamwise flow visualizations are illustrated in Fig. 4.12. It appears that the boundary layers over the inner surfaces of the doors interact with the shear layer. Flow separation and vortex generation around the doors are observed in Fig. 4.12. These flow separations, vortex generations and interactions look stronger towards the aft wall of the cavity, at $x/L = 0.95$, in the following figure.

In the outer regions of the doors, door boundary layers and plate are in strong interaction, which also trigger corner flow in these regions.

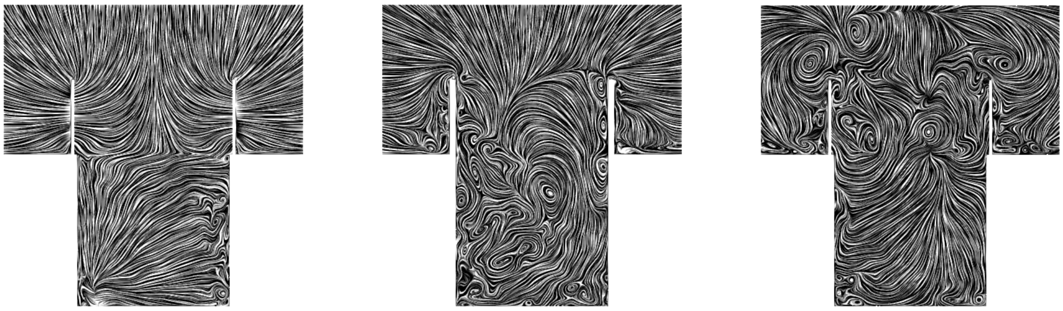

$x/L = 0.05$ $x/L = 0.5$ $x/L = 0.95$

Figure 4.12: Instantaneous streamwise LIC images for cavity doors at 90°

Flow visualizations in spanwise planes are shown in Fig. 4.13. With the doors at 90° orientation, vortex structures spanning the cavity length look to get weaker. Also, there exist many smaller vortices toward the back of the cavity.

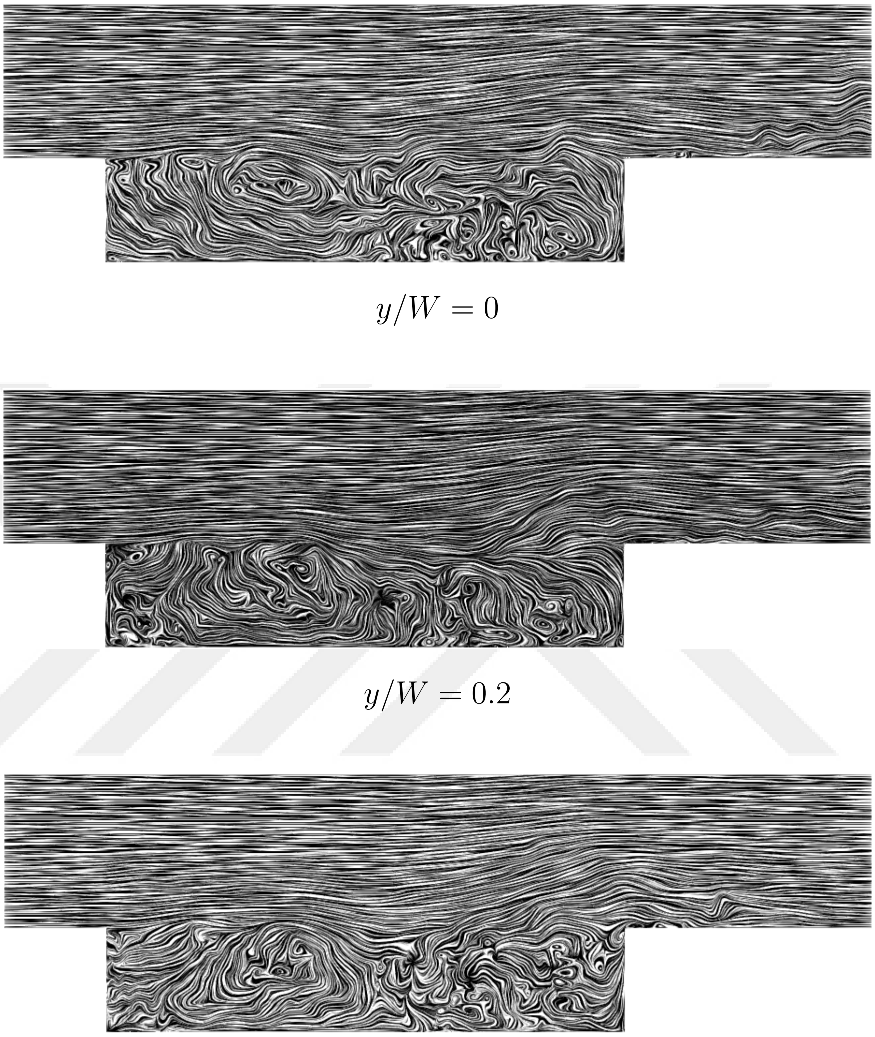

$y/W = 0$

$y/W = 0.2$

$y/W = 0.4$

Figure 4.13: Instantaneous spanwise LIC images for cavity doors at 90°

Therefore, the cavity doors at 90° configuration causes significant changes in flow physics in comparison to the clean cavity configuration. Strong interactions develop in all three directions. The effects of the doors appear up in the acoustic environment of the cavity. From all these results, we conclude that the presence of doors significantly affects the flow around the cavity.

The computed acoustic results with the 90° door position are compared with the available experimental data [31] in Fig. 4.14 to assure the suitability of the computational method to this type of situation, as well. It is evident in Fig. 4.14a that the IDDES results for the doors-open case appear to agree with the OASPL measurements quite well. Also, pressure spectrum is also predicted quite accurately in terms of both the modal amplitudes and the frequencies as illustrated in Fig. 4.14b. Therefore, IDDES approach for the rest of the doors-open cases will be continued to be used.

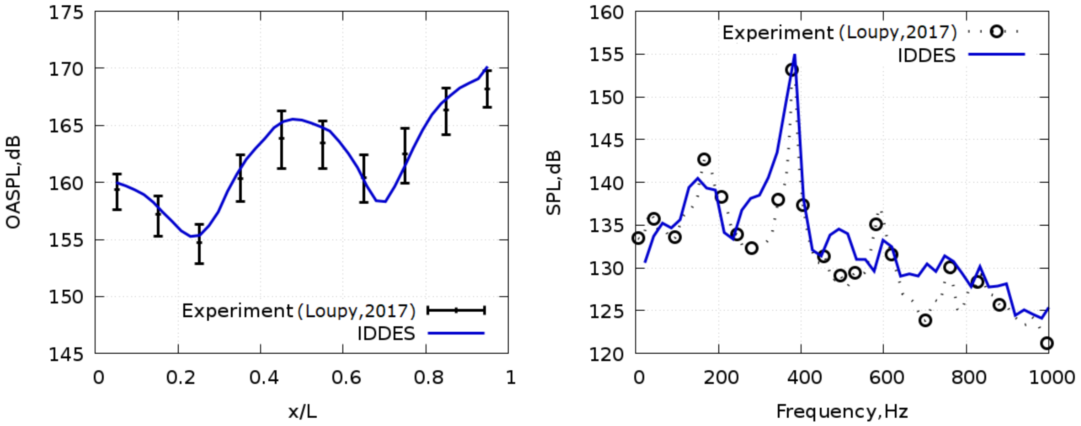

(a) OASPL

(b) Pressure spectrum at $x/L = 0.95$

Figure 4.14: Acoustic characteristics of 90° doors configuration

4.1.3.2 Doors Orientation Effects

Following the validation of computational methodology for the cavity with 90° open doors, other door positions are also analyzed for better understanding of the effects of the deployed doors. The OASPL along the cavity ceiling centerline for doors at 60° and 120° are compared to those with 90° door position, as well as to the clean cavity results in Fig. 4.15a. It can be observed from the figure that the doors either at 60° or at 90° significantly change the OASPL along the cavity ceiling centerline. On the other hand, noise intensity trend of 120° doors configuration is quite similar to the clean cavity although it causes increased noise levels. The doors affect the acoustic characteristics especially around the front wall region and mid-section of the cavity, causing significant increase in the noise levels.

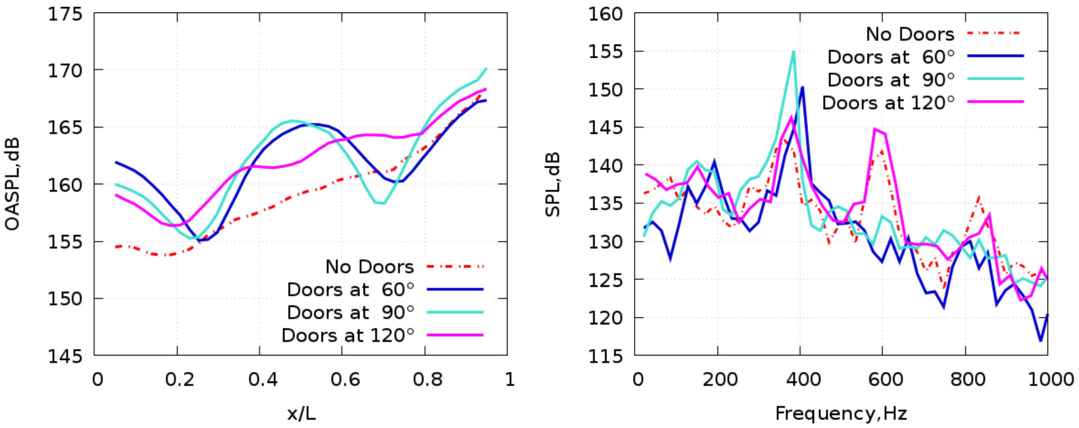

(a) OASPL

(b) Pressure spectrum at $x/L = 0.95$

Figure 4.15: Effects of cavity doors angle on the acoustic characteristics along the cavity ceiling centerline

Both 60° and 90° orientations yield similar trends in OASPL with ω-like distribution along the cavity length. The doors at 90° orientation result in the highest OASPL around the aft wall of the cavity. On the other hand, 60° orientation of the doors does not cause any increase in OASPL at the back of the cavity. Unlike the aft region, 60° orientation of the doors causes the highest OASPL in the front region. Although doors at 120° cause an increase in the noise intensity along the cavity ceiling centerline, effects of the doors get weaker as the orientation angle of the doors increases towards 120° orientation.

Frequency spectra of doors at 60° and 120° are compared to doors at 90° and the clean cavity as shown in Fig. 4.15b. Doors at 60° and 90° alignments completely change the modal structure of the cavity. The 3^{rd} mode at $\sim$ 600 Hz almost disappears while the 2^{nd} mode at $\sim$ 390 Hz increases in magnitude with no significant frequency change. Pressure spectrum of 120° configuration is also quite similar to the clean cavity. This shows that 120° alignment of the doors has relatively weaker affects on the cavity flow due to relatively weakened interactions compared to other doors orientations considered.

Flow visualizations for the cavity with 60° door position are shown in Fig. 4.16. Acoustic waves are confined more into the interior of the cavity compared to the 90° doors case. The boundary layer flow of the doors, cavity walls and the generated shear layer all interact with the acoustic waves within the cavity. As it is illustrated in the figure, the wakes of doors are in stronger interaction than in the 90° doors case.

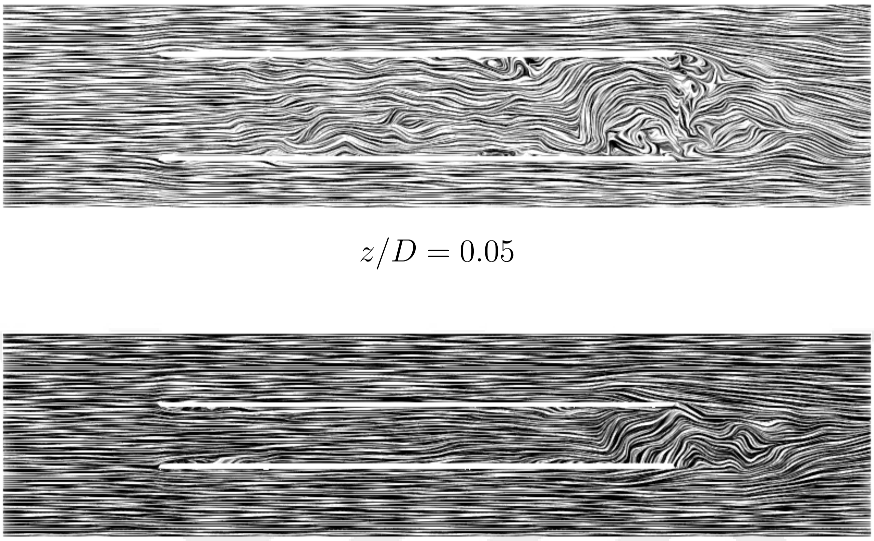

$z/D = 0.05$

$z/D = 0.45$

Figure 4.16: Instantaneous LIC images at $z/D = 0.05$ and $z/D = 0.45$ for cavity doors at 60°

In the outer regions of the doors, boundary layers over them and the plate are in weaker interaction because of the higher angle between the doors and plate. Therefore, the corner flows in these regions are not as strong as in 90° doors case, and the flow around these joints is not governed by vortices.

Spanwise flow patterns exhibit the doors affect explicitly as shown in Fig. 4.17. In the symmetry plane of cavity at $y/W = 0$, flow seeps out of the cavity between the doors towards the aft wall of the cavity. This leakage of the flow towards outside cavity weakens the noise intensity in that region, by energizing the shear layer in the attachment region on the aft wall. As spanwise location gets closer to $y/W = 0.4$ plane, which is the closest plane to the cavity side wall, flow starts to be packed within the cavity. At $y/W = 0.4$ plane, flow is almost completely confined within the cavity, which enhances the interactions.

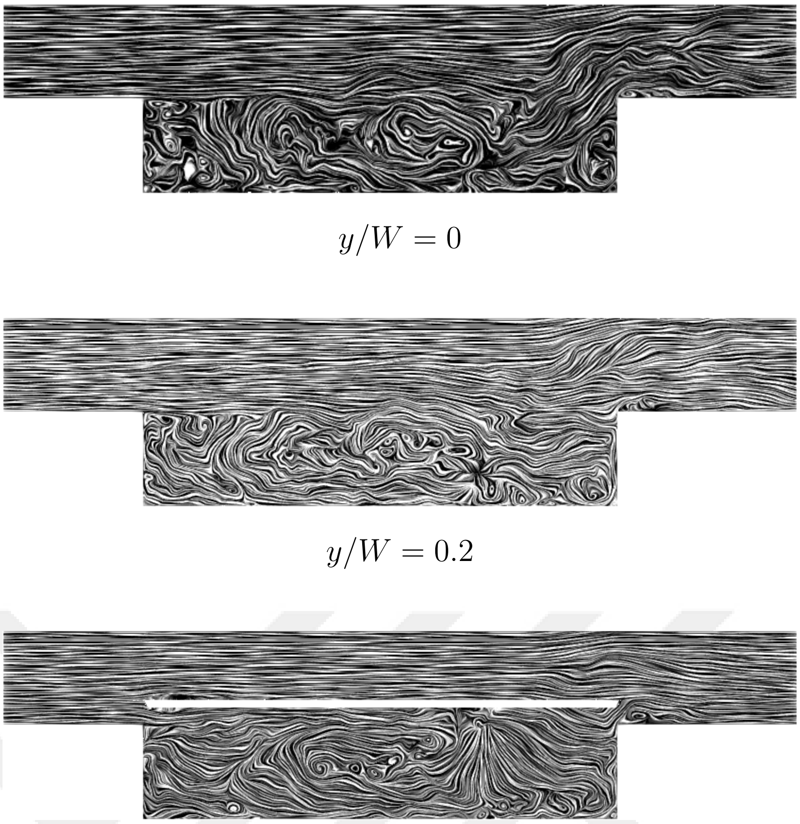

$y/W = 0$

$y/W = 0.2$

$y/W = 0.4$

Figure 4.17: Instantaneous spanwise LIC images for cavity doors at 60°

Streamwise flow visualizations are illustrated in Fig. 4.18 for 60° doors orientation. The boundary layer over the inner surfaces of the doors interacts with the shear layer causing separation, and vortex generation around the doors. The flow around the doors is dominated by vortical flow structures.

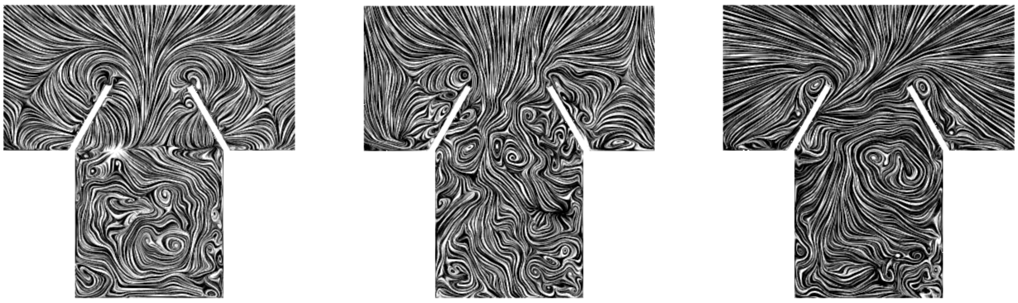

$x/L = 0.05$ $x/L = 0.5$ $x/L = 0.95$

Figure 4.18: Instantaneous streamwise LIC images for cavity doors at 60°

The effects of the doors at $120°$ on the spanwise flow patterns are explicitly shown in Fig. 4.19. Doors at $120°$ orientation allows rather smooth acoustic waves propagation outside the cavity. Therefore, weaker acoustic-flow interactions shows up in the spanwise flow patterns that the flow field is less affected by doors at $120°$ orientation.

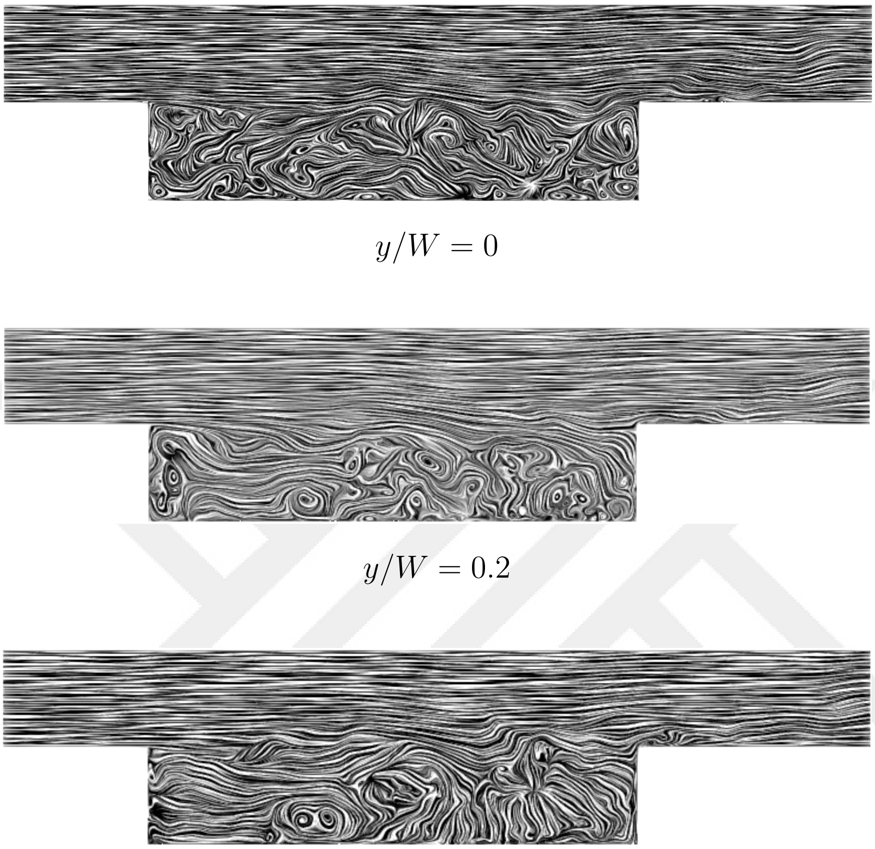

$y/W = 0$

$y/W = 0.2$

$y/W = 0.4$

Figure 4.19: Instantaneous spanwise LIC images for cavity doors at $120°$

Streamwise flow visualizations for the cavity with $120°$ door position are shown in Fig. 4.20. The interactions between the boundary layers over the inner surfaces of the doors with the shear layer are also weaker. On another note, boundary layers of outer surfaces of the doors and the plate are in close contact that give rise to strong interactions. Therefore, the flow around the joints is mainly governed by vortices.

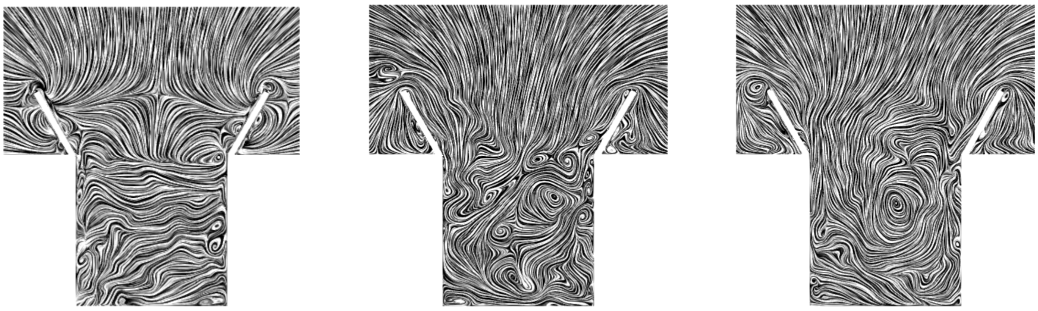

$x/D = 0.05$ $x/D = 0.5$ $x/D = 0.95$

Figure 4.20: Instantaneous streamwise LIC images for cavity doors at $120°$

Flow visualizations around the doors are shown in Fig. 4.21. With the increased orientation angle of the doors at $120°$ configuration, confinement of acoustic waves is not as strong as neither $60°$ nor $90°$ orientations. Interactions between the boundary layer flows of the doors, and cavity walls and the generated shear layer are relatively weaker in doors at $120°$ orientation.

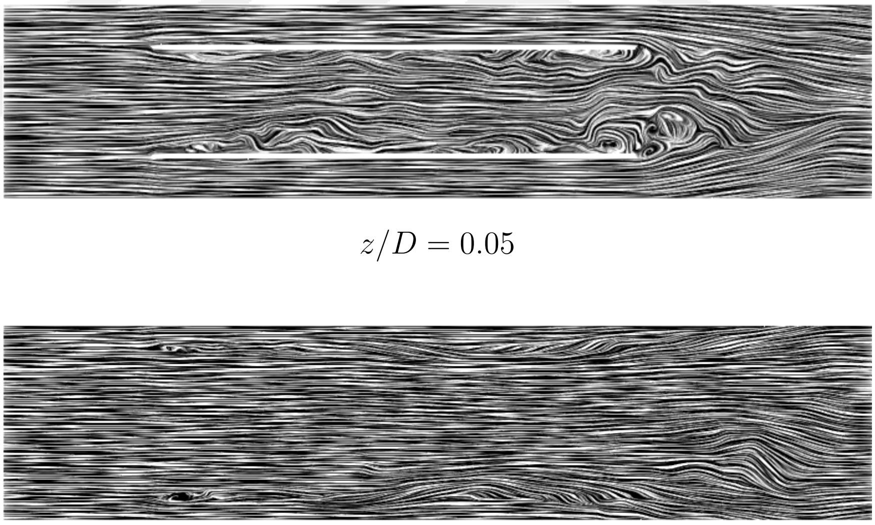

$z/D = 0.05$

$z/D = 0.45$

Figure 4.21: Instantaneous LIC images at $z/D = 0.05$ and $z/D = 0.45$ for cavity doors at $120°$

As an overall conclusion, the doors at $90°$ configuration inherently affects the flow field because of the strong interactions between the boundary layer over the inner surfaces of doors, the shear layer and the acoustic waves, which reflects in between the doors. In the doors at 60° alignement, the acoustic waves are more restricted to the interior region of the cavity. This results in extended effects of presence of the doors on the cavity flow. Further, doors at 120° orientation is more efficient acoustically due to weaker interactions of the boundary layers of the doors, the shear layer and the acoustic waves.

4.1.4 Reynolds Number Dependency of Cavity Flows

It is well known that characteristics of turbulent flow are highly dependent on Reynolds number. Turbulent intensity of a flow is determined by Reynolds number, which is proportional to boundary layer thickness. In cavity flows, separated boundary layer at the leading edge of the cavity drives the shear layer generation and hence, it directly affects the acoustic characteristics of cavity flows. Therefore, Reynolds number dependency of cavity acoustics is questioned in this section.

M219 clean cavity is considered as the base geometry, whose operating Reynolds number is 6.5×10^6, based on cavity length. Reynolds numbers of 13×10^6 and 26×10^6 are also analyzed. These Reynolds numbers are obtained by scaling the cavity in all three dimensions. For each Reynolds number, re-meshing is done with the same grid properties.

OASPL and P_{rms} comparisons for Reynolds numbers considered are illustrated in Fig. 4.22a and Fig. 4.22b, respectively. It is observed that Reynolds number inversely affects the OASPL along the cavity ceiling centerline. That is, OASPL decreases with increasing Reynolds number although decrement is not significant. General trend for each of Reynolds numbers is similar.

Reynolds number dependency of pressure spectrum at $x/L = 0.95$ is shown in Fig. 4.22b with respect to non-dimensional frequency, Strouhal number (St). It is observed that modal frequencies and peak amplitudes for 6.5×10^6 and 13×10^6 are quite similar. For Re $= 26 \times 10^6$, amplitudes of the 1^{st} and 4^{th} mode are amplified. 2^{nd} and 3^{rd} modes are in consistence for all of Reynolds numbers considered.

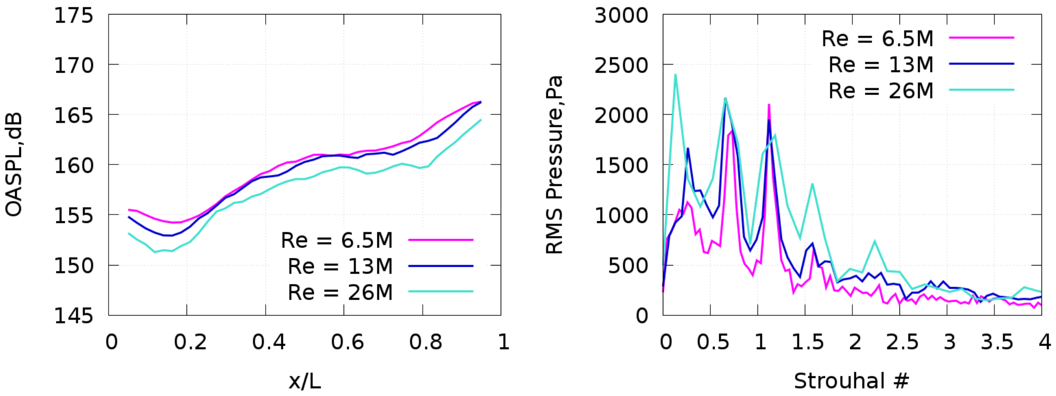

(a) OASPL (b) RMS Pressure at $x/L = 0.95$

Figure 4.22: Reynolds number effect on transonic open cavity flows ($M = 0.85$)

As a conclusion, Reynolds number does not cause any significant change in the cavity acoustic environment. Therefore, small scale cavity geometries can be used for representation of real scale internal weapon bays. This result is crucial because it is not easy to test large scale geometries. Even it is quite expensive to simulate high Re flows in CFD environment.

4.2 Farfield Noise Prediction By Ffowcs Williams - Hawkings Acoustic Analogy

One of the important parameters in determination of cavity acoustic environment is the farfield noise characteristics. Noise is generated as a result of cavity flow, which propagates in the free stream of air. Noise levels at a distance $15 \times L$ (cavity length) are computed via in-house Ffowcs Williams - Hawkings (FW-H) acoustic analogy Fortran code. The results for farfield noise levels are illustrated in Fig. 4.23.

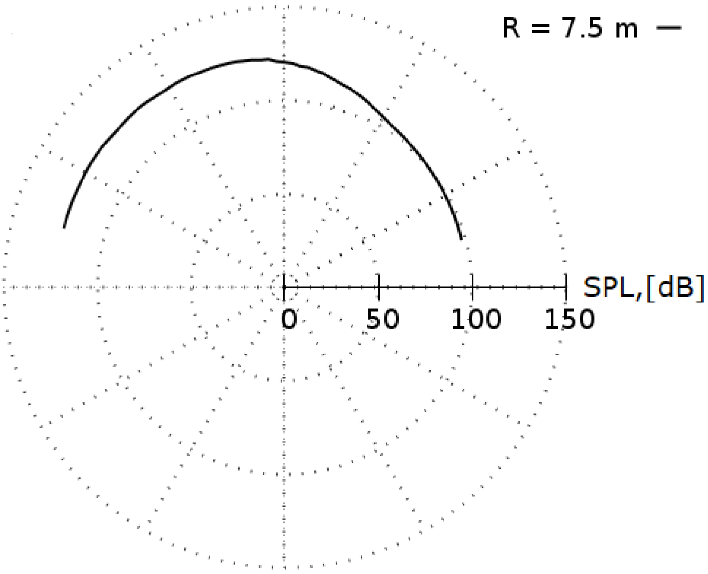

Figure 4.23: Noise prediction at $15 \times L$ distance from the cavity trailing edge centerline via FW-H acoustic analogy method

It is observed that farfield noise propagation has upstream directivity. Acoustic waves generated on the aft wall of the cavity due to shear layer re-attachment propagate upstream within and around the cavity. This propagation in upstream direction is also observed in the farfield of the cavity. Farfield noise levels significantly decrease compared to near region of the cavity due to absorption by air and increased distance from the sound source, which is the cavity flow basically.

CHAPTER 5

CONCLUSIONS

In this thesis, highly turbulent flowfields of a transonic open type cavity with and without doors as well as with and without a store are studied via computational fluid dynamics (CFD). Solutions are obtained in a time accurate manner to determine the highly dynamic loads in the cavity environment. The unsteady pressure data from the computed fields are post-processed to find the overall sound pressure levels (OASPL) and frequency dependent pressure fluctuations. Radiated sound is also predicted from the clean cavity configuration.

Computational studies are carried out first on a clean cavity configuration with various levels of turbulence modeling to evaluate their ability for predicting such highly turbulent fields. The turbulence modeling approaches included the usual URANS k-ω SST and RNG k-ϵ, and ultimately Detached Eddy Simulation (DES) approach, delayed DES (DDES) approach and its improved delayed DES (IDDES) variant. It is found that the predicted OASPL on the centerline of the cavity ceiling using the k-ω SST model has high dependence on meshing, although the RNG k-ϵ model produces similar results on the different resolution meshes used. Though, both the RNG k-ϵ and k-ω SST models capture the general trends of OASPL distributions within a few dB of the available experimental data. On the contrary, both of these models cannot capture the pressure spectrum with an acceptable accuracy. More specifically, these models only appear to be successful in prediction of the modal frequencies, not the peak amplitudes in the spectrum. Sensitivity of the k-ω SST model to the order of the numerical scheme is more distinct compared to that of the RNG k-ϵ model. Unlike the k-ω SST model, the RNG k-ϵ produces similar results for both noise intensity and pressure spectrum within the cavity. Therefore, it is concluded that, among the URANS approaches tests the RNG k-ϵ model performs relatively better in cavity flow solutions, and these models can be used only in the preliminary assessment of the cavity flow noise intensity. URANS approaches should not be employed when higher fidelity predictions are needed.

As aforementioned in solutions of the cavity flow problems in this thesis, DES, delayed DES (DDES), and improved delayed DES (IDDES) are also utilized. These are supposed to provide more accurate solutions. It is indeed observed that the IDDES method provides the best predictions for the clean cavity configuration. The model is able capture the OASPL and pressure spectrum within the cavity with a quite acceptable accuracy. It also provides the best approximation of the shear layer streamwise velocity profile in comparison to the experimental measurements.

While all these effects of the turbulence modeling are studied, influence of the time step size is also assessed. A time step size of $\Delta t = 1 \times 10^{-5}$ s appears a good compromise between the accuracy and computational cost for this type of solutions. From all these assessment studies, it is concluded that the IDDES method with a times step size of $\Delta t = 1 \times 10^{-5}$ s on 17-25 million element meshes provides the highest accuracy for cavity flow solutions among the other turbulence models of interest in the present work. Following the study to find the best combinations of the CFD model, mesh and time step size resolutions, more detailed analyses of cavity configurations, including the doors and stores are carried out, are carried out. It is concluded that IDDES turbulence modeling approach with 3^{rd} order numerical discretization and $\Delta t = 1 \times 10^{-5}$ s time step with an appropriate computational grid performs quite reasonable accuracy in prediction of cavity acoustic environment at transonic speeds for various cavity configurations.

First, the clean cavity is analyzed in more detail. More specifically flowfield visualizations in the cavity volume as well as cavity walls are carried out to understand the flow physics more. Results indicate that the cavity ceiling and aft wall OASPL distributions provide non-significant OASPL distributions along offset planes at $y/W = 0$, $y/W = 0.2$, and $y/W = 0.4$. However, OASPL distributions over the front wall of the cavity appear more severe, and the levels increase towards both the cavity opening and side walls.

Following the clean cavity study, a generic store is aft mounted within the cavity to identify the effects of presence of the store. This configuration appears to produce comparable noise intensity to the clean cavity along the cavity ceiling centerline. Therefore, we conclude that the presence of the store within the cavity does not exhibit any significant change in the acoustic environment of the cavity.

Final configuration studied is the doors-on cavity. Analyses for door positions of 60°, 90° and 120° to the cavity opening plane are conducted. The outcome is that the presence of doors seriously affects the cavity acoustics. All of the configurations result in an increase in OASPL almost all along the cavity centerline. Although all of the configurations have serious impact, 90 deg alignment of the doors causes the most severe change in the acoustic field within the cavity. This is mainly due to confinement of the spanwise dynamics of the shear layer as well as acoustics between doors and the cavity walls. Doors at 120° orientation results in OASPL trend close to the clean cavity configuration although it causes an increase in noise intensity along the centerline of the cavity ceiling.

One of the outcomes of this thesis is the conclusion that the computational models utilized have the capability to predict the acoustic environment of various cavity configurations such as cavity with a store, cavity with doors and etc. The power of the computational model implies its applicability to simulate real internal weapon bay geometries. In other words, the algorithm outlined in this thesis can be utilized in simulation of acoustic environment of real internal weapon bay geometries.

Appendix A

GRID SIZE AND COMPUTATIONAL COST APPROXIMATIONS FOR DNS AND LES

A.1 DNS Resolution

DNS aims to resolve the Kolmogorov scales in a turbulent flow. Therefore, it requires a computational grid resolution that is smaller than Kolmogorov scale, η, which results in tremendous amount of grid size. Computational cost of DNS is proportional to Kolmogorov length and time scales. For a mixing layer, number of grid points for a DNS solution is approximated by [3]:

$$N_x N_y N_z \sim (L/\eta)^3 \sim \mathrm{Re}^{9/4} \tag{A.1.1}$$

Reynolds number dependence of the grid resolution for wall bounded flows is much stricter because of the appropriate scaling requirement of the near wall turbulent eddies. Governing equations must be integrated in time for integral time scale, T, while time step satisfies both CFL and Kolmogorov time scale, τ_η, simultaneously:

$$N_t \sim T/\Delta t \sim L/\eta \sim \mathrm{Re}^{3/4} \quad N_t \sim T/\Delta t \sim L/\eta \sim \mathrm{Re}^{1/2} \tag{A.1.2}$$

Overall computational cost of the model approximates:

$$N_x N_y N_z \times N_t \sim \mathrm{Re}^{11/4} \rightarrow \mathrm{Re}^3 \tag{A.1.3}$$

A.2 LES Resolution for Wall Bounded Flows

In LES, only the integral scales are resolved and smaller scales are modeled. Therefore, it is sufficient for LES to use approximately 20-30 grid points in each direction in space. The assumption is that grid size in all directions is a fixed fraction of δ.

$$N_xN_yN_z \sim N_{\text{cubes}} \sim (L/\delta)^2 \tag{A.2.1}$$

where L/δ varies with Re because of the B/L thickness, δ, dependence on Re.

A.2.1 Outer Layer

In outer layer resolution requirement of LES method, L/δ dependence on Re is relatively weak ($\sim$ Re$^{0.2}$) that gives:

$$N_xN_yN_z \sim N_{\text{cubes}} \sim (L/\delta)^2 \sim \text{Re}^{0.4} \tag{A.2.2}$$

and the total computation cost for outer layer calculations is approximated as:

$$N_xN_yN_z \times N_t \sim \text{Re}^{0.6} \tag{A.2.3}$$

A.2.2 Inner Layer

Within the inner layer, near-wall eddies must be resolved. In the inner layer, grid size must be constant in wall units. Streamwise and spanwise grid sizes are approximated by $\Delta x \approx 100$, $\Delta z \approx 20$. Towards outer layers, grid sizes can be relaxed. Grid point size is approximated by:

$$N_xN_yN_z \sim \text{Re}^{1.8} \tag{A.2.4}$$

and the total computation cost for inner layer calculations is approximated as:

$$N_xN_yN_z \times N_t \sim \text{Re}^{2.4} \tag{A.2.5}$$

There is a stronger dependency on Re for inner layer. This means that massively separated flows are more affordable in terms of computational cost. For attached B/L flows, inner layer of LES model will require special treatment that results in a significant grid size increase.

Appendix B

TURBULENCE MODELS DETAILS

B.1 URANS Additional Equations

$$\overline{\sigma_{ij}} = \overline{2\mu\left(S_{ij} - \frac{1}{3}S_{kk}\delta_{ij}\right)} \approx 2\widetilde{\mu}\left(\widetilde{S_{ij}} - \frac{1}{3}\widetilde{S_{kk}}\delta_{ij}\right) \tag{B.1.1}$$

where S_{ij} is the strain tensor.

Reynolds stress tensor, R_{ij}, in URANS equations is given by:

$$\overline{R_{ij}} = \overline{\rho u_i u_j} - \overline{\rho}\widetilde{u_i}\widetilde{u_j} = \overline{\rho}(\widetilde{u_i u_j} - \widetilde{u_i}\widetilde{u_j}) \tag{B.1.2}$$

Favre (density-weighted) average is given by ; $\widetilde{\phi} = \overline{\rho\phi}/\bar{\rho}$, with $\phi = \bar{\phi} + \phi' = \widetilde{\phi} + \phi''$.
Total energy and total enthalpy formulations in URANS equations are given as:

$$\begin{aligned} \widetilde{E} &= c_\nu\widetilde{T} + \frac{\overline{\rho}\widetilde{u_i}\widetilde{u_i}}{2} + \frac{R_{ii}}{2\overline{\rho}} \\ \widetilde{H} &= c_p\widetilde{T} + \frac{\overline{\rho}\widetilde{u_i}\widetilde{u_i}}{2} + \frac{R_{ii}}{2\overline{\rho}} \end{aligned} \tag{B.1.3}$$

The heat fluxes are given as:

$$\begin{aligned} \overline{q_j} &= -\overline{k_T\frac{\partial T}{\partial x_j}} \approx -\widetilde{k_T}\frac{\partial \widetilde{T}}{\partial x_j} \\ \overline{Q_j} &= \overline{\rho}c_p(\widetilde{u_j T_t} - \widetilde{u_j}\widetilde{T_t}) \end{aligned} \tag{B.1.4}$$

where T_t is the total temperature.
The equation of state is given by:

$$\bar{p} = (\gamma - 1)\left[\bar{p}\widetilde{E} - \frac{1}{2}\bar{\rho}(\widetilde{u}^2 + \widetilde{v}^2 + \widetilde{w}^2) - \bar{\rho}k\right] \tag{B.1.5}$$

where γ, the heat capacity of air, is taken constant as 1.4 and k is the turbulent kinetic energy, obtained by:

$$k = [\widetilde{(u_i^{\text{“}})}^2 + \widetilde{(v_i^{\text{“}})}^2 + \widetilde{(w_i^{\text{“}})}^2]/2 \tag{B.1.6}$$

B.2 k-ω SST Turbulence Model Additional Equations and Model Constants

The turbulent eddy viscosity, μ_t, is computed from;

$$\mu_t = \frac{\rho a_1 k}{\max(a_1\omega, \Omega F_2)} \tag{B.2.1}$$

Each constant is composed of an inner (1) and outer (2) constant, from;

$$\phi = F_1\phi_1 + (1 - F_1)\phi_2 \tag{B.2.2}$$

The additional functions used in Eq.B.1.5 and Eq. B.1.6 are given as follows:

$$\begin{aligned} F_1 &= \tanh(\arg_1^4) \\ \arg_1 &= \min\left[\max\left(\frac{\sqrt{k}}{\beta^*\omega d}, \frac{500\nu}{d^2\omega}\right), \frac{4\rho\sigma_{\omega 2}k}{CD_{k\omega}d^2}\right] \\ CD_{k\omega} &= \max\left(2\rho\sigma_{\omega 2}\frac{1}{\omega}\frac{\partial k}{\partial x_j}\frac{\partial \omega}{\partial x_j}, 10^{-20}\right) \\ F_2 &= \tanh(\arg_2^2) \\ \arg_2 &= \max\left(\frac{\sqrt{k}}{\beta^*\omega d}, \frac{500\nu}{d^2\omega}\right) \end{aligned} \tag{B.2.3}$$

where the model constants for the inner (SST model), i.e inside the boundary layer, and outer (k-ϵ model), i.e outside the boundary layer, are;

$\sigma_{k1} = 0.85$	$\sigma_{\omega 1} = 0.5$	$\beta_1 = 0.075$
$\sigma_{k2} = 1.0$	$\sigma_{\omega 2} = 0.856$	$\beta_2 = 0.0828$
β^*=0.09	$\kappa = 0.41$	$a_1 = 0.31$

B.3 RNG k-ϵ Turbulence Model Additional Equations and Model Constants

Turbulent kinetic energy production term, G_k is given by:

$$G_k = -\rho\overline{u_i' u_j'}\frac{\partial u_j}{\partial x_i} \tag{B.3.1}$$

Effective viscosity is a result of scale elimination procedure of RNG theory, whch gives a differential equation for turbulent viscosity:

$$d\left(\frac{\rho^2 k}{\sqrt{\epsilon\mu}}\right) = 1.72\frac{\widetilde{\nu}}{\sqrt{\widetilde{\nu}^3 - 1 + C_\nu}}d\widetilde{\nu} \tag{B.3.2}$$

where $\widetilde{\nu} = \mu_{\text{eff}}/\mu$ and $C_\nu \approx 100$.

In high Reynolds numbers, turbulent viscosity term takes the form:

$$\mu_t = \rho C_\mu \frac{k^2}{\epsilon} \tag{B.3.3}$$

with $C_\mu = 0.0845$ from RNG theory.

Since swirling or rotation affects the turbulent characteristics of the flow, turbulent viscosity term, μ_t can be redefined to account for swirl effects:

$$\mu_t = \mu_{t0} f\left(\alpha_s, \Omega, \frac{k}{\epsilon}\right) \tag{B.3.4}$$

where μ_{t0} is the non-swirling turbulent viscosity, Ω is the characteristic swirl number, and α_s is the swirl constant.

Inverse Prandtl Numbers

Inverse Prandtl numbers in RNG k-ϵ model, α_k and α_ϵ, are given as:

$$\left|\frac{\alpha - 1.3929}{\alpha_0 - 1.3929}\right|^{0.6321} \left|\frac{\alpha - 2.3929}{\alpha_0 - 2.3929}\right|^{0.3679} = \frac{\mu_{\text{mol}}}{\mu_{\text{eff}}} \tag{B.3.5}$$

where $\alpha_0 = 1.0$. In high Reynolds number limit, $\mu_{\text{mol}}/\mu_{\text{eff}} \ll 1$ and $\alpha_k = \alpha_\epsilon \approx 1.393$.

R_ϵ term in ϵ equation is:

$$R_\epsilon = \frac{C_\mu \rho \eta^3 (1 - \eta/\eta_0)}{1 + \beta \eta^3} \frac{\epsilon^2}{k} \tag{B.3.6}$$

where $\eta \equiv Sk/\epsilon$, $\eta_0 = 4.38$, $\beta = 0.012$.

The model constants for RNG k-ϵ equation are:

$$C_{1\epsilon = 1.42} \quad \text{and} \quad C_{2\epsilon = 1.68} \tag{B.3.7}$$

B.4 Sutherland's Law of Dynamic Viscosity

Sutherland's law of dynamic viscosity is based on the kinetic theory, by Sutherland (1893), which states that dynamic viscosity of air is dependent on the air temperature, with regard to the intermolecular forces between the air molecules. Sutherland's law is given as:

$$\mu = \mu_{\text{ref}} \left(\frac{T}{T_{\text{ref}}}\right)^{3/2} \frac{T_{\text{ref}} + S}{T + S} \tag{B.4.1}$$

where

$T_{\text{ref}} = 273.11\ K$; reference static temperature
$\mu_{\text{ref}} = 1.716 \times 10^{-5}\ kg/m \cdot s$; dynamic viscosity at temperature T_{ref}
$S \quad = 110.56\ K$; Sutherland's constant implying an effective temperature

B.5 Spalart-Almaras (S-A) One-Equation Turbulence Model

Turbulent eddy viscosity in Spalart-Almaras (S-A) one equation model is computed from:

$$\mu_t = \rho \widetilde{\nu} f_{\nu 1} \tag{B.5.1}$$

with

$$f_{\nu 1} = \frac{X^3}{X^3 + c_{\nu 1}^3}, and \quad X = \frac{\widetilde{\nu}}{\nu} \tag{B.5.2}$$

Additional definitions for S-A model are as follows:

$$\begin{aligned} f_{\nu 2} = 1 - \frac{X}{1 + X f_{\nu 1}} \quad f_\omega &= g \left[\frac{1 + c_{\omega 3}^6}{g^6 + c_{\omega 3}^6}\right]^{1/6} \\ g &= r + c_{\omega 2}(r^6 - r) \\ r &= \min \left[\frac{\widetilde{\nu}}{\widetilde{S} \kappa^2 d^2}, 10\right] \\ f_{t2} &= c_{t3} \text{exp}(-c_{t4} X^2) \\ W_{ij} &= \frac{1}{2}\left(\frac{\partial u_i}{\partial x_j} - \frac{\partial u_j}{\partial x_i}\right) \end{aligned} \tag{B.5.3}$$

The boundary conditions are:

$$\widetilde{\nu}_{\text{wall}} = 0, \quad \widetilde{\nu}_{\text{farfield}} = 3\nu_\infty : to : 5\nu_\infty \tag{B.5.4}$$

which corresponds to:

$$\nu_{t,\text{wall}} = 0, \quad \nu_{t,\text{farfield}} = 0.210438\nu_\infty : to : 1.294234\nu_\infty \tag{B.5.5}$$

Model constants are:

$c_{b1} = 0.1135$ $\sigma = 2/3$ $c_{b2} = 0.622$ $\kappa = 0.41$

$c_{\omega 2} = 0.3$ $c_{\omega 3} = 2$ $c_{\nu 1} = 7.1$ $c_{t3} = 1.2$

$c_{t4} = 0.5$ $c_{\omega 2} = \frac{c_{b1}}{\kappa^2} + \frac{1+c_{b2}}{\sigma}$

YÖK

Appendix C

DATA PROCESSING DETAILS

C.1 Fast Fourier transform (FFT)

Fast Fourier transform (FFT) is a signal processing algorithm used to convert discrete time domain data to its discrete frequency domain representation. FFT is useful in aeroacoustics for reading modal frequencies and power of fluctuations at modal peaks.

Unlike the conventional FFT, which strictly requires data with power of 2, FFT implemented in Fluent utilizes prime-factor algorithm. Prime-factor FFT algorithm accepts any products of 2, 3, 4, 5, 6, 7, 8, 9, 11, 13, and 16, which provides the algorithm flexibility to preserve the original data better.

Discrete Fourier transform of a time domain data, $P(t)$, with a finite number of data is represented by $P(f)$ and given by:

$$P(f) = \sum_{n=0}^{N-1} \hat{P}_n e^{2\pi ikn/N} \quad k = 0, 1, 2, ...(N-1) \tag{C.1.1}$$

where $\hat{P}_n$ are the Fourier coefficients obtained from:

$$\hat{P}_n = \frac{1}{N} \sum_{k=0}^{N-1} P_k e^{2\pi ikn/N} \quad n = 0, 1, 2, ...(N-1) \tag{C.1.2}$$

C.2 Windowing

FFT algorithm assumes time domain data set converted to frequency domain corresponds to a continuous spectrum that repeats periodically. This implies matching first and last data points. In real life applications, as in the cavity acoustics, discrete data is not composed of integer number of periods. This violates the assumption of repeating periodicity of the signal and causes discontinuities, which can introduce high frequency components that are not present originally. These frequencies can exceed Nyquist frequency and result in aliasing in the spectrum.

To minimize the non-integer number of periods in FFT, some techniques are available called ”windowing”. Windowing becomes involved in reducing the amplitudes of discontinuities in at the boundaries of each sequence utilized in FFT. This forces endpoints of consecutive sequences to meet and act like a continuous data. Windowing minimizes the aliasing and artificial high frequency components insertion.

Consider a time domain data with length N and sampling rate Δt.

$$P_k \equiv P(t_k), \quad t_k \equiv k\Delta t, \quad k = 0, 1, 2, ...(N-1) \tag{C.2.1}$$

Original input data, P_j is multiplied by a windowing function, W_j, to window the input data.

$$\widetilde{P_j} = P_j W_j \quad j = 0, 1, 2, ...(N-1) \tag{C.2.2}$$

There are many of windowing functions existent. In the present study, Hanning window is utilized because of its adequate frequency resolution and reduced spectral leakage. Windowing function, W_j, for Hanning window is given as follows:

$$W_j = \begin{cases} 0.5[1-\cos(\frac{8\pi j}{N})] & j \leq \frac{N}{8},\, j \geq \frac{7N}{8} \\ 1 & \frac{N}{8} < j < \frac{7N}{8} \end{cases} \tag{C.2.3}$$

A sample to Hanning window with 50% overlap is given in Fig. C.1.

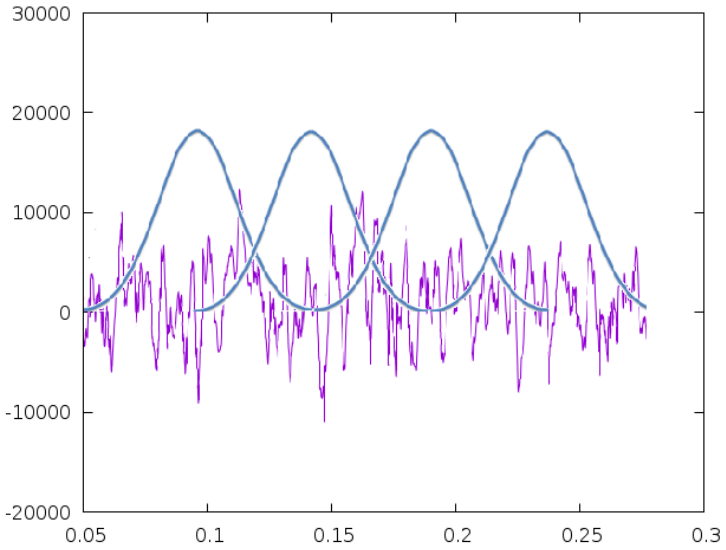

Figure C.1: Hanning window with 0.5 overlap

YÖK

REFERENCES

[1] ESDU, "Aerodynamics and aero-acoustics of rectangular planform cavities. Part I: time-averaged flow. Technical Report 02008," tech. rep., ESDU International, 2004.

[2] P. Sagaut, S. Deck, and M. Terracol, *Multiscale And Multiresolution Approaches In Turbulence*. Imperial College Press, 2013.

[3] U. Piomelli, "Large eddy simulation lecture notes." the von Karman Institute for Fluid Dynamics Lecture Series, May 2018.

[4] P. Nayyar, G. N. Barakos, and K. J. Badcock, "Analysis and control of transonic cavity flow using DES and LES," *35th AIAA Fluid Dynamics Conference and Exhibit*, 2005.

[5] J. A. Ross and J. Peto, "The effect of cavity shaping, front spoilers and ceiling bleed on loads acting on stores, and on the unsteady environment within weapon bays," tech. rep., QinetiQ, 1997.

[6] K. Knowles, D. Bacci, A. J. Saddington, B. Newby, and N. J. Taylor, "Controlling unsteady cavity flows using internal structures," in *Proc. 52nd 3AF International Conference on Applied Aerodynamics*, (Lyon, France), 2017.

[7] D. P. Rizzetta and M. R. Visbal, "Large-eddy simulation of supersonic cavity flow fields including flow control," *International Journal of Aeronautical and Space Sciences*, vol. 16, no. 1, pp. 19,27, 2015.

[8] Y. Liu and M. Tong, eds., *Aeroacoustic Investigation of a Cavity with and without Doors by Delayed Detached Eddy Simulation*, 2018.

[9] D. H. Kim, J. H. Choi, and O. J. Kwon, "Detached eddy simulation of weapons bay flows and store separation," *International Journal of Aeronautical and Space Sciences*, vol. 16, no. 1, pp. 19,27, 2015.

[10] R. Nichols, "Detached eddy simulation of weapons bay flows and store separation," *Comparison of Hybrid Turbulence Models for a Circular Cylinder and a Cavity*, vol. 44, no. 6, pp. 1207,1219, 2006.

[11] B. E. Launder and N. D. Sandham, *Closure Strategies for Turbulent and Transitional Flows*, ch. Introduction to Large Eddy Simulation of Turbulent Flows, pp. 267–298. Cambridge University Press, 2002.

[12] F. Menter, "Two-equation eddy-viscosity turbulence models for engineering applications," *AIAA Journal*, vol. 32, pp. 1598–1605, 1994.

[13] J. E. Bardina, P. G. Huang, and T. J. Coakley, "Turbulence modeling validation, testing, and development," *NASA Technical Memorandum*, 1997.

[14] D. A. Johnson and L. S. King, "Mathematically simple turbulence closure model for attached and separated turbulent boundary layers," *AIAA Journal*, vol. 23, pp. 1684–1692, 1985.

[15] P. R. Spalart, S. Deck, M. L. Shur, K. Squires, M. K. Strelets, and A. Travin, "A new version of detached-eddy simulation, resistant to ambiguous grid densities," *Theor. Comput. Fluid Dyn.*, vol. 20, pp. 181–195, 2006.

[16] M. L. Shur, P. R. Spalart, M. K. Strelets, and A. K. Travin, "A hybrid RANS-LES approach with delayed-DES and wall-modeled LES capabilities," *International Journal of Heat and Fluid Flow*, vol. 29, pp. 1638–1649, 2008.

[17] N. V. Nikitin, F. Nicoud, B. Wasistho, K. D. Squires, and P. Spalart, "An approach to wall modeling in large-eddy simulations," *Physics of Fluids*, vol. 12, pp. 1629–1632, 2000.

[18] F. Menter and M. Kuntz, "Adaptation of eddy-viscosity turbulence models to unsteady separated flow behind vehicles," tech. rep., Ansys-CFX, 2004.

[19] C. Mockett, *A comprehensive study of detached-eddy simulation*. PhD thesis, Technischen Universität Berlin, 2009.

[20] H. Liu, C. Yan, Y. Zhao, and Y. Qin, "Analysis of pressure fluctuation in transonic cavity flows modal decomposition," *Aerospace Science and Technology*, 2017.

[21] K. Luo and Z. Xiao, “Improved delayed detached-eddy simulation of transonic and supersonic cavity flows,” *Progress in Hybrid RANS-LES Modelling, Notes on Numerical Fluid Mechanics and Multidisciplinary Design*, vol. 130, 2015.

[22] E. K. Guseva, “Analysis of pressure fluctuation in transonic cavity flows modal decomposition,” *Journal of Physics: Conference Series*, vol. 769, 2016.

[23] M. S. Gritskevich, A. V. Garbaruk, J. Schutze, and F. R. Menter, “Development of ddes and iddes formulations for the k-ω shear stress transport model,” *Flow, Turbulence and Combustion*, vol. 88(3), pp. 431–449, 2012.

[24] J. E. F. Williams and D. L. Hawkings, “Sound generation by turbulence and surfaces in arbitrary motion,” *Royal Society Publishing*, vol. 264, pp. 321–341, 1969.

[25] K. S. Brentner and F. Farassat, “Analytical comparison of the acoustic analogy and Kirchoff formulation for moving surfaces,” *AIAA*, vol. 36, 1998.

[26] A. N. Yazdi, G. A. Bres, and L. Mongeau, “An acoustic analogy formulation for moving sources in uniformly moving media,” *Proceedings of the Royal Society*, vol. 467, pp. 144–165, 2011.

[27] F. Farassat, “Derivation of formulations 1 and 1a of farassat,” tech. rep., NASA, 2007.

[28] J. A. Rossiter, “Preliminary investigation into armament bay buffet at subsonic and transonic speeds,” tech. rep., Royal Aircraft Establishment, 1960.

[29] H. Heller, D. Holmes, and E. Covert, “Flow induced pressure oscillations in shallow cavities,” *Journal of Sound and Vibration*, vol. 18(4), pp. 545–553, 1970.

[30] G. J. M. Loupy and G. N. Barakos, eds., *Understanding Transonic Weapon Bay Flows*, 7th European Conference on Computational Fluid Dynamics (ECFD 7). Glasgow,UK, 2018.

[31] G. J. M. Loupy, G. N. Barakos, and N. J. Taylor, “Cavity flow over a transonic weapons bay during door operation,” *Journal of Aircraft*, vol. 55, pp. 339–354, 2017.